

THE STELLAR METALLICITY DISTRIBUTION FUNCTION OF THE GALACTIC HALO FROM SDSS PHOTOMETRY

DEOKKEUN AN¹, TIMOTHY C. BEERS^{2,3}, JENNIFER A. JOHNSON⁴, MARC H. PINSONNEAULT⁴, YOUNG SUN LEE^{3,5,11},
JO BOVY^{6,12}, ŽELJKO IVEZIĆ⁷, DANIELA CAROLLO^{8,9}, AND MATTHEW NEWBY¹⁰

¹ Department of Science Education, Ewha Womans University, Seoul 120-750, Republic of Korea; deokkeun@ewha.ac.kr

² National Optical Astronomy Observatory, Tucson, AZ 85719, USA

³ Department of Physics & Astronomy and JINA (Joint Institute for Nuclear Astrophysics), Michigan State University, E. Lansing, MI 48824, USA

⁴ Department of Astronomy, Ohio State University, 140 West 18th Avenue, Columbus, OH 43210, USA

⁵ Department of Astronomy, New Mexico State University, Las Cruces, NM 88003, USA

⁶ Institute for Advanced Study, Einstein Drive, Princeton, NJ 08540, USA

⁷ Department of Astronomy, University of Washington, Box 351580, Seattle, WA 98195, USA

⁸ Macquarie University Research Centre in Astronomy, Astrophysics & Astrophotonics,
Department of Physics & Astronomy, Macquarie University, NSW 2109, Australia

⁹ INAF-Osservatorio Astronomico di Torino, Strada Osservatorio 20, Pino Torinese, I-10020 Torino, Italy

¹⁰ Department of Physics, Applied Physics and Astronomy, Rensselaer Polytechnic Institute Troy, NY 12180, USA

Received 2012 June 12; accepted 2012 November 27; published 2013 January 8

ABSTRACT

We explore the stellar metallicity distribution function of the Galactic halo based on SDSS *ugriz* photometry. A set of stellar isochrones is calibrated using observations of several star clusters and validated by comparisons with medium-resolution spectroscopic values over a wide range of metal abundance. We estimate distances and metallicities for individual main-sequence stars in the multiply scanned SDSS Stripe 82, at heliocentric distances in the range 5–8 kpc and $|b| > 35^\circ$, and find that the in situ photometric metallicity distribution has a shape that matches that of the kinematically selected local halo stars from Ryan & Norris. We also examine independent kinematic information from proper-motion measurements for high Galactic latitude stars in our sample. We find that stars with retrograde rotation in the rest frame of the Galaxy are generally more metal poor than those exhibiting prograde rotation, which is consistent with earlier arguments by Carollo et al. that the halo system comprises at least two spatially overlapping components with differing metallicity, kinematics, and spatial distributions. The observed photometric metallicity distribution and that of Ryan & Norris can be described by a simple chemical evolution model by Hartwick (or by a single Gaussian distribution); however, the suggestive metallicity–kinematic correlation contradicts the basic assumption in this model that the Milky Way halo consists primarily of a single stellar population. When the observed metallicity distribution is deconvolved using two Gaussian components with peaks at $[\text{Fe}/\text{H}] \approx -1.7$ and -2.3 , the metal-poor component accounts for $\sim 20\%$ – 35% of the entire halo population in this distance range.

Key words: Galaxy: abundances – Galaxy: evolution – Galaxy: formation – Galaxy: halo – Galaxy: stellar content

Online-only material: color figures

1. INTRODUCTION

Knowledge of the nature of the stellar Galactic halo, which collectively preserves a detailed record of our Galaxy’s formation in the early universe (e.g., Eggen et al. 1962; Searle & Zinn 1978), has expanded a great deal in the past few years. With the advent of large photometric surveys such as the Sloan Digital Sky Survey (SDSS; York et al. 2000; Stoughton et al. 2002; Abazajian et al. 2003, 2004, 2005, 2009; Gunn et al. 2006; Adelman-McCarthy et al. 2006, 2007, 2008; Aihara et al. 2011), as well as the massive spectroscopic follow-up efforts that have come from SDSS, in particular, the Sloan Extension for Galactic Understanding and Exploration (SEGUE; Yanny et al. 2009), and the recently completed SEGUE-2 extension (C. Rockosi et al., in preparation), the opportunity to collect a vast amount of information on the nature of the Galactic halo has arrived. Detailed quantitative comparisons of these observations with the spatial, kinematical, and chemical space inferred from theoretical predictions of models for the formation of the stellar halo through the hierarchical merging of higher-mass subhalos

and accretion of lower-mass subhalos (e.g., Bullock & Johnston 2005; Johnston et al. 2008; Font et al. 2011; McCarthy et al. 2012; Tissera et al. 2012) are now within reach.

Much attention has been paid to understanding the nature of the stellar halo(s), in terms of the chemical and kinematical properties of its constituent stars. For example, based on the medium-resolution SDSS spectroscopy of “local” halo stars ($d_{\text{helio}} < 4$ kpc), Carollo et al. (2007, 2010) argued that our Milky Way stellar halo is a superposition of two overlapping systems, the inner and outer halos, that are distinct in metallicity, kinematics, and spatial distributions (see also Beers et al. 2012). Furthermore, Nissen & Schuster (2010) showed that high $[\alpha/\text{Fe}]$, metal-poor halo stars in the solar neighborhood are mainly on prograde orbits, while those with low $[\alpha/\text{Fe}]$ abundances are preferentially found on retrograde orbits. High $[\alpha/\text{Fe}]$ halo stars are likely associated with a dissipative component of the Galaxy that experienced a rapid chemical evolution, while the low $[\alpha/\text{Fe}]$ stars could be accreted components from dwarf galaxies that had lower star formation rates. For example, one could point toward low-mass (low-metallicity) dwarf-like galaxies (surviving examples of which might include the ultra-faint dwarfs discovered by SDSS, e.g., Willman et al. 2005; Belokurov et al. 2006a, 2006b; Zucker et al. 2006, and many

¹¹ Tombaugh fellow.

¹² Hubble fellow.

others since; see also the discussion of Carollo et al. 2012 and Qian & Wasserburg 2012) as likely progenitors of the outer-halo stellar population of the Milky Way.

The key observational ingredient in testing and studying the dual nature of the Galactic halo is the metal abundance for individual stars. In particular, such a diversity of stellar populations in the halo could have been imprinted on the metallicity distribution function (MDF) of halo stars. Previous results on the halo MDFs have been based primarily on spectroscopic surveys of likely halo stars selected from kinematically biased (e.g., Ryan & Norris 1991b; Carney et al. 1996) or kinematically unbiased (e.g., the HK survey of Beers et al. 1985, 1992; the Hamburg/ESO survey described by Christlieb 2003 and Christlieb et al. 2008) searches for metal-poor stars. These approaches have the advantage of identifying stars of the lowest metallicity reasonably efficiently, which are of great interest in their own right, but they suffer from selection biases that can be difficult to quantify. Biases are of particular importance if one seeks to understand the global properties of the stellar halo, a necessary step in order to tell a coherent story of the assembly and evolution of large spiral galaxies such as the Milky Way. In this regard, large photometric surveys such as SDSS can be used to recover relatively unbiased information on the nature of the Galactic halo.

Broadband photometry can provide reasonably accurate estimates of stellar metallicities, temperatures, and distances, at least for main-sequence stars. In the pioneering work to recover stellar metallicities from SDSS *ugriz* photometry, Ivezić et al. (2008a) devised a method of using polynomial regressions based on spectroscopic calibrations of de-reddened $u - g$ and $g - r$ colors (see also Peng et al. 2012), which is similar to the traditional method of relating UV excess with positions on the Johnson *UBV* diagrams (e.g., Carney 1979). The clear advantage of using a photometric metallicity technique is the efficiency of estimating metallicities for main-sequence stars, which are the most plentiful and representative sample of individual stellar populations.

As recognized by Ivezić et al. (2008a), the polynomial-based photometric metallicity technique that they developed becomes quite insensitive at lower metallicity. They compared photometrically estimated metallicities with those obtained for a subset of the same sample of stars with available spectroscopic determinations, and found that the photometric $[\text{Fe}/\text{H}]$ estimates effectively saturate at $[\text{Fe}/\text{H}]_{\text{spec}} \lesssim -2$, and cannot be extended to lower metallicities due to limits placed by the level of photometric errors obtained by SDSS.

Although the power of photometric metallicity determinations from broadband colors is fundamentally limited at low metallicities, metallicity estimates can indeed be pushed down to below $[\text{Fe}/\text{H}] \sim -2.5$, through the use of well-defined color-metallicity relations. For example, in An et al. (2009a), we used theoretical isochrones, calibrated using sets of observed cluster data, to estimate photometric metallicities for a large number of stars in the halo, based on SDSS *gri* photometry. Although individual metallicity estimates exhibit significant errors, due to the weak metallicity sensitivity of *gri* colors, it was shown that application of the calibrated isochrones can extend the low-metallicity limit down to at least $[\text{Fe}/\text{H}] \sim -2.5$, based on a comparison with SDSS spectroscopic abundance measurements.

In this paper, we extend our previous efforts on the calibration of stellar isochrones to provide improved photometric metallicity estimates, taking into account the full set of information from the SDSS *ugriz* measurements (Section 2). A newly calibrated

set of isochrones is developed, superseding the set discussed by An et al. (2009b). Based on these new isochrones, we re-explore application of the photometric metallicity estimation technique (which is clearly independent of that discussed previously by Ivezić et al. 2008a) to samples of stars with available SDSS photometry (Section 3), in order to construct an unbiased MDF of the Galactic halo (Section 4). Based on our derived photometric MDFs and a limited investigation of available kinematic information, we show that simple chemical evolution models that are assumed to apply to a single stellar population provide inadequate descriptions of the nature of the Galactic halo.

2. PHOTOMETRIC METALLICITY TECHNIQUE

The key ingredient for photometric estimation of stellar metallicities (as well as distances) is the use of well-established stellar color-magnitude relations over a wide range of stellar atmospheric parameters. For this purpose, we adopted the formalism in An et al. (2009b), where we used a set of YREC (Sills et al. 2000) stellar isochrones in the SDSS filter system calibrated against observed *ugriz* (open and globular) cluster photometry (An et al. 2008) to estimate the stellar metallicities and distances of individual stars.

As an initial exploration of this technique, we used the SDSS *gri* data to constrain (median) photometric metallicities (hereafter $[\text{Fe}/\text{H}]_{\text{phot}}$) for bulk stellar populations in the halo (An et al. 2009a). However, it was necessary to include *u*-band measurements to tightly constrain photospheric metal abundances and therefore to construct a precise MDF. This has a consequence of limiting the application of the photometric technique to nearby main-sequence stars, because of the relatively shallow survey limit in the SDSS *u* passband ($u = 22.0$ at the 95% detection repeatability for point sources).

In this section, we describe the development of empirical corrections to color- T_{eff} relations for stellar isochrones in the native SDSS filter system (An et al. 2009b), including the *u* passband, and test the accuracy of color- T_{eff} relations and photometric metallicities using spectroscopic estimates from the SEGUE Stellar Parameter Pipeline (SSPP; Lee et al. 2008a, 2008b; Allende Prieto et al. 2008; Smolinski et al. 2011)

2.1. Background: Calibration of Isochrones

In the following analysis, we employ the same set of underlying stellar interior models and the same α -element enhancement scheme as in An et al. (2009b), motivated by the observed behavior of these elements among field dwarfs and cluster stars from spectroscopic studies (e.g., Venn et al. 2004; Kirby et al. 2008): $[\alpha/\text{Fe}] = +0.4$ at $[\text{Fe}/\text{H}] = -3.0$, $[\alpha/\text{Fe}] = +0.3$ at $[\text{Fe}/\text{H}] = -2.0, -1.5, -1.0$, $[\alpha/\text{Fe}] = +0.2$ at $[\text{Fe}/\text{H}] = -0.5$, and $[\alpha/\text{Fe}] = +0.0$ at $[\text{Fe}/\text{H}] = -0.3, -0.2, -0.1, +0.0, +0.1, +0.2, +0.4$. A linear interpolation was made in this metallicity grid to obtain isochrones at intermediate $[\text{Fe}/\text{H}]$ values. We adopted an age of 13 Gyr for $-3.0 \leq [\text{Fe}/\text{H}] \leq -1.2$, and 4 Gyr at $-0.3 \leq [\text{Fe}/\text{H}] \leq +0.4$, with a linear interpolation between these two metallicity ranges. As described below, our strategy minimizes the application of our calibrated stellar models to main-sequence turnoff stars, for which colors are most sensitive to the adopted age. For this reason, our main results are insensitive to the age assumption, but readers are cautioned if they apply our models to stellar populations with different ages. The above age-metallicity- $[\alpha/\text{Fe}]$ relations are adopted throughout this paper.

Colors and magnitudes predicted by theoretical models typically do not agree with those observed from star clusters. Therefore, we defined color- T_{eff} -[Fe/H] corrections to better match the data. In An et al. (2009b), we used M67 cluster data to define color- T_{eff} relations in $u - g$, $g - r$, $g - i$, and $g - z$, at the cluster’s metal abundance ([Fe/H] = 0.0). In An et al. (2009a), we adopted these correction factors in gri color indices at solar abundance, and used a linear ramp between [Fe/H] = -0.8 and [Fe/H] = 0.0. In this weighting scheme, empirical corrections become zero at [Fe/H] = -0.8 and below, so metallicity estimation of metal-poor stars are essentially those obtained from pure theoretical calculations, and are not affected by the empirical color corrections. This choice was motivated by the fact that the models are in satisfactorily agreement with data in gri color indices for globular clusters (An et al. 2009b). Above solar abundance, we applied the M67-based color corrections to all models, assuming that offsets in colors between the model and data are independent of the metal abundance of a star.

2.2. Updates: Calibration of Isochrones

In principle, cluster sequences alone can be used to directly estimate stellar distances and metallicities, as long as there exist well-measured cluster-star samples over a wide range of [Fe/H]. However, cluster data are often noisy (e.g., some cluster fiducials are found to be essentially superimposed, even if their [Fe/H] values are different), so we choose instead to be guided by theory, in order to infer stellar colors at any given metallicity (and/or age; see also An et al. 2007a, 2007b; Pinsonneault et al. 2004).

In particular, updates on the empirical calibrations of models were necessary to adjust model $u - g$ colors, which have a profound impact on the accuracy of photometric metallicity estimates, to better match observed cluster fiducial sequences over a wide range of metal abundances. Below we describe our adopted methodology used to generate a new set of calibrated isochrones for all of the $ugriz$ color indices.

We expanded upon the strategy of An et al. (2009b) for the color- T_{eff} calibration by the addition of cluster fiducial sequences in An et al. (2008) over a wide range of metal abundances. Although our pure theoretical models predict colors that are consistent with observed fiducial sequences within the total systematic and random errors (An et al. 2009b), there still remains a small, but suggestive systematic residual pattern of the color offsets over T_{eff} and [Fe/H]. In the updated calibration set, we have attempted to minimize these effects to better constrain estimates of the stellar parameters.

In the color- T_{eff} -[Fe/H] calibration, which is described in detail below, we used cluster fiducial sequences for several globular and open clusters in An et al. (2008). These clusters are listed in Table 2, along with our adopted values for the cluster parameters, which are the same as those used in our earlier model comparisons (An et al. 2008). The [Fe/H] and $E(B - V)$ estimates for globular clusters are from Kraft & Ivans (2003), who used Fe II lines from high-resolution spectra to compare colors derived from high-resolution spectroscopic determinations of T_{eff} with the observed colors of the same stars. Distances to the globular clusters are all *Hipparcos*-based subdwarf fitting distances. We adopted the Carretta et al. (2000) distance estimates whenever they are available, since they employed the same metallicity scale for both subdwarfs and cluster stars in the subdwarf-fitting technique; otherwise, we adopted distances in Kraft & Ivans (2003). For M67, we took the average reddening and metallicity estimates from high-resolution spectroscopy

Table 1
Photometric Zero-point Differences

Cluster	SDSS	UberCa1 - Photo				
		$\langle\Delta u\rangle$	$\langle\Delta g\rangle$	$\langle\Delta r\rangle$	$\langle\Delta i\rangle$	$\langle\Delta z\rangle$
M15	2566	0.020	0.007	-0.005	-0.006	-0.010
M15	1739	0.008	0.003	-0.005	0.003	-0.009
M92	4682	-0.037	-0.013	-0.010	-0.015	-0.034
M92	5327	-0.001	-0.004	-0.031	-0.035	-0.026
M13	3225	0.011	-0.003	-0.001	-0.005	0.006
M13	3226	0.007	-0.011	-0.006	-0.002	0.007
M3	4646	0.039	0.014	0.016	0.010	0.008
M3	4649	-0.022	0.011	0.013	0.004	-0.015
M5	1458	-0.002	-0.005	-0.001	0.004	-0.001
M5	2327	-0.010	-0.001	-0.007	0.008	0.019
M67	5935	-0.002	0.001	-0.002	0.001	-0.004
M67	5972	0.004	-0.001	-0.001	0.007	-0.009
NGC 6791	5416	0.003	0.003	0.004	0.004	0.008
NGC 6791	5403	0.001	0.001	0.001	0.000	0.000

in the literature (An et al. 2007b and references therein), and adopted a cluster distance estimated from an empirically calibrated set of isochrones in the Johnson-Cousins-2MASS system (An et al. 2007b). For NGC 6791, we adopted the average [Fe/H] from high-resolution spectroscopic studies (see references in An et al. 2009b). The cluster’s reddening and distance estimates are based on the application of our calibrated isochrones in the Johnson-Cousins-2MASS system (D. An et al., in preparation).

We employed UberCa1 (Uber-calibration) magnitudes (Padmanabhan et al. 2008) for calibrating the cluster systems, instead of the “Photometric Telescope (PT)”-calibrated magnitudes (hereafter Photo magnitudes).¹³ Our original cluster sequences in An et al. (2008) were on the Photo system, where the standard SDSS photometric pipeline (Lupton et al. 2002) was used to define stellar colors and magnitudes in SDSS. However, Padmanabhan et al. (2008) later devised a method of improving a relative photometric calibration error by using repeat measurements in the overlapping fields of the survey. Since DR7, SDSS takes the UberCa1 magnitudes as the default magnitudes.

We transformed the fiducial sequences in the Photo system onto the UberCa1 system, by applying zero-point differences between the two systems in the cluster flanking fields, where we derived photometric zero points for the cluster fiducials (An et al. 2008). The differences between the two calibrations are not alarmingly large for the fiducial sequences used in the current study. The mean differences are $+0.003 \pm 0.014$ mag, $+0.003 \pm 0.015$ mag, -0.001 ± 0.010 mag, -0.005 ± 0.028 mag, and -0.003 ± 0.013 mag in $ugriz$, respectively, in the sense of UberCa1 minus Photo magnitudes, for all the cluster fields considered in An et al. (2008), except from the few imaging stripes from which we could not retrieve UberCa1 magnitudes. The zero-point differences between UberCa1 and Photo systems for several cluster fields used in this work are listed in Table 1.

Gray cross points in Figures 1–4 represent the color differences between cluster fiducial sequences and pure theoretical stellar models in $g - r$, $g - i$, $g - z$, and $u - g$, respectively. In each of the color indices, we have arranged the comparisons such that comparisons for metal-poor clusters are shown in the upper panels, and those for metal-rich clusters are shown in

¹³ See also <http://www.sdss3.org/dr8/algorithms/fluxcal.php>.

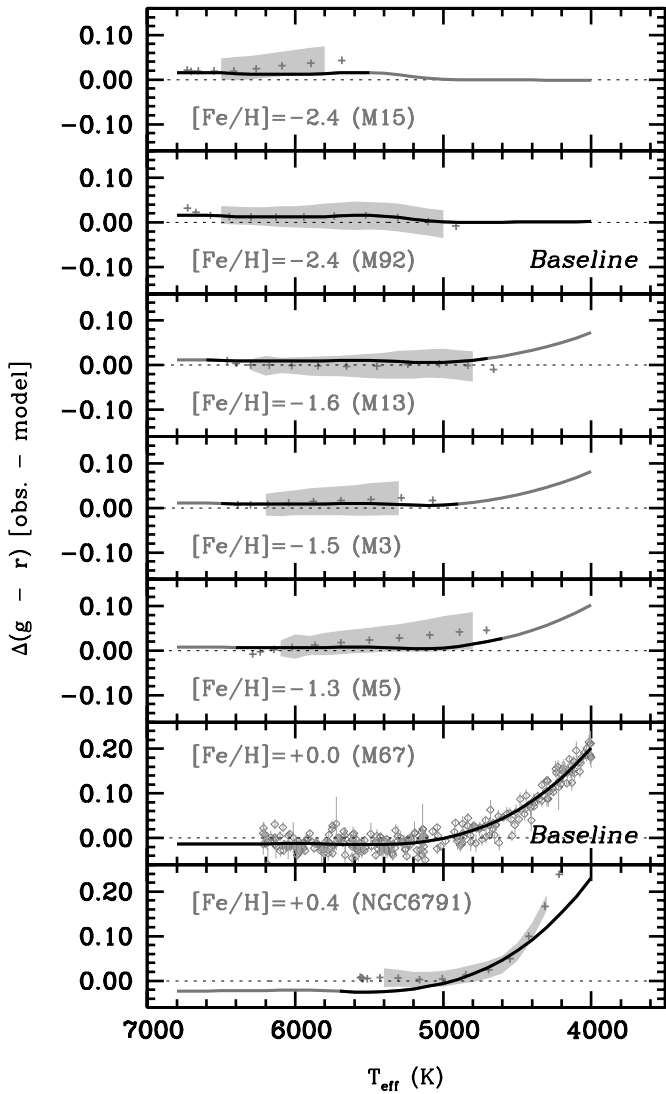


Figure 1. Updated color- T_{eff} - $[\text{Fe}/\text{H}]$ calibrations of YREC isochrones. Gray cross points are color differences in $g-r$ between the YREC models and cluster fiducial sequences. A gray strip represents a $\pm 1\sigma$ range of a total systematic error in the comparison. Individual cluster cases are displayed in increasing order of metallicity from the upper to lower panels. Solid lines represent our derived color- T_{eff} - $[\text{Fe}/\text{H}]$ corrections, based on all of the cluster comparisons shown above, where M92 and M67 comparisons are used as a baseline (see the text). Color differences for individual stars are shown for M67.

the lower panels. A gray strip represents a $\pm 1\sigma$ range of a total systematic error in the comparison, including errors from the distance, reddening, age, and an assumed photometric zero-point error on the fiducial sequences (see also An et al. 2008 for more details).

Solid lines in Figures 1–4 show empirical color corrections derived using cluster fiducial sequences. We based our calibration using cluster fiducial sequences for both M92 and M67. In other words, color- T_{eff} relations were defined with the observed main sequences of M92 at $[\text{Fe}/\text{H}] = -2.4$ (Kraft & Ivans 2003), and those at $[\text{Fe}/\text{H}] = 0.0$ were defined with respect to M67 (see An et al. 2007b). The choice of M92 and M67 for the base case was due to the fact that these clusters are well studied and have reliably determined distances, foreground reddening, and metallicity estimates (An et al. 2009b, see also Table 2). They both also have wide T_{eff} coverage (see Figures 1–4).

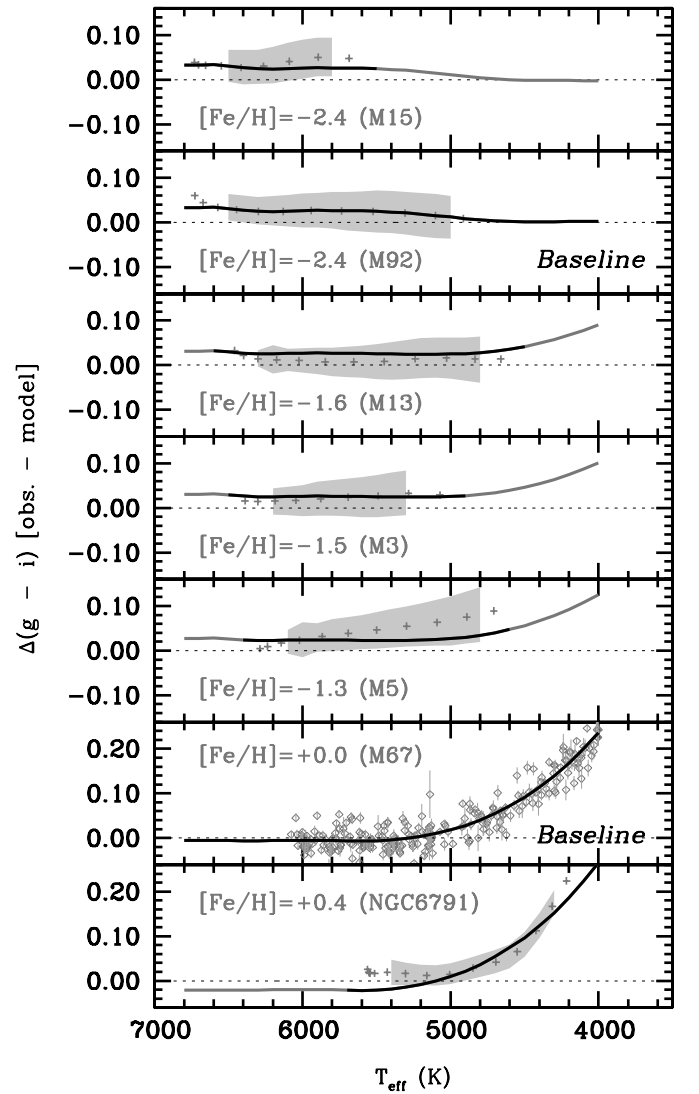


Figure 2. Same as in Figure 1, but for $g-i$.

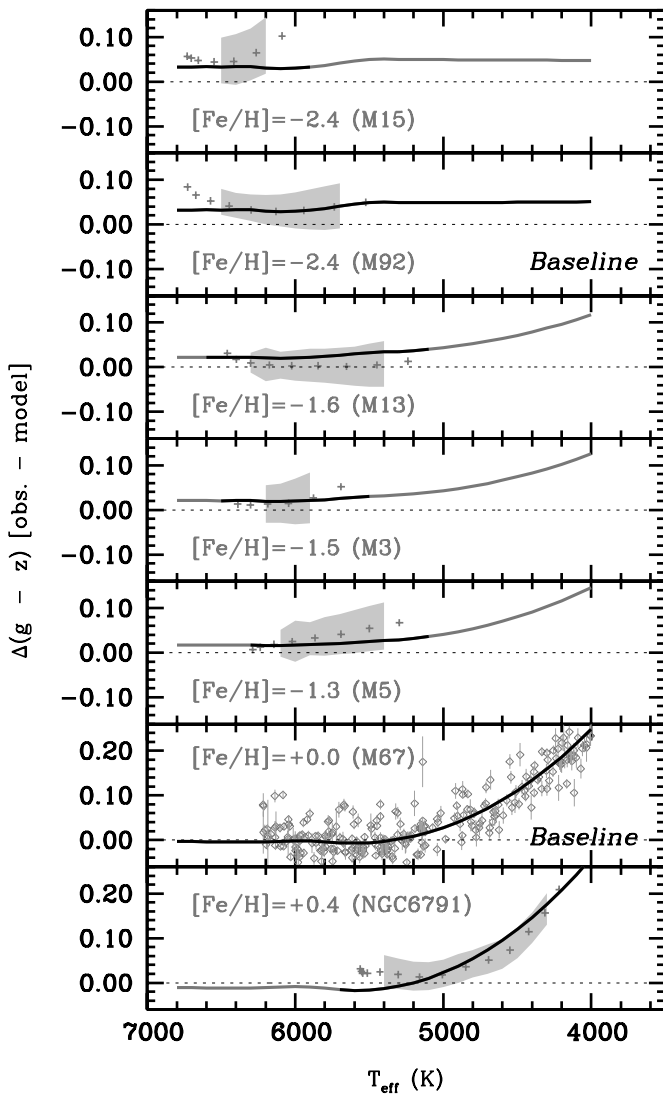
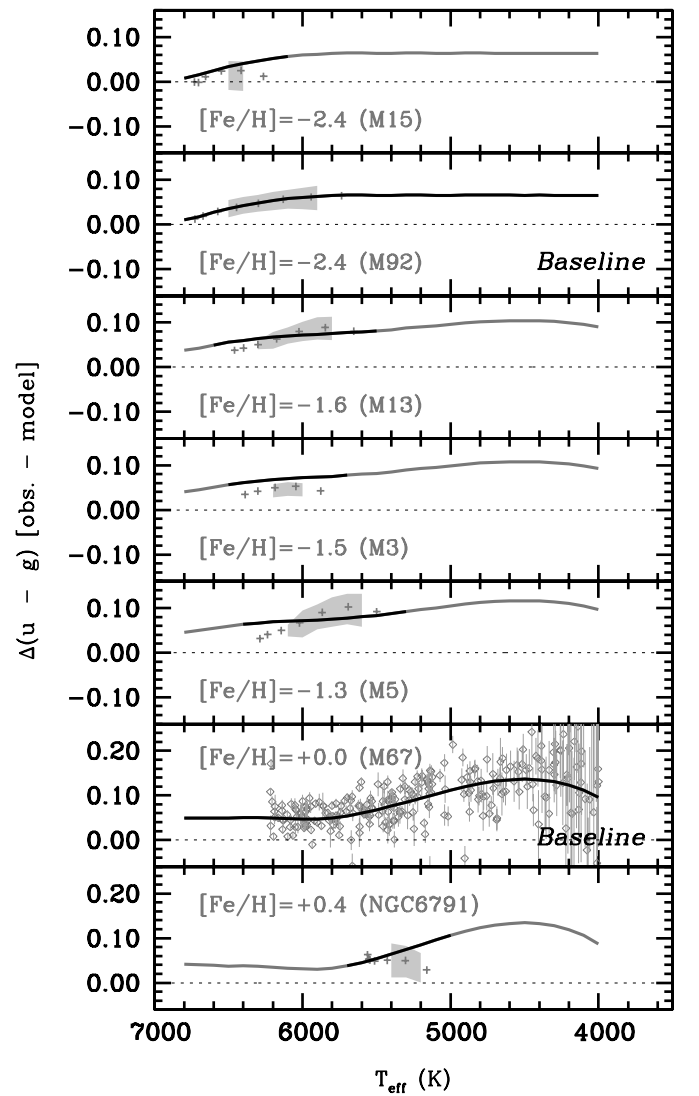
Table 2
Adopted Cluster Parameters

Cluster Name	$(m - M)_0$ (mag)	$E(B - V)$ (mag)	$[\text{Fe}/\text{H}]$ (dex)	Age ^a (Gyr)	References
M15	15.25	0.10	-2.42	12.6	1
M92	14.64	0.02	-2.38	12.6	1, 2
M13	14.38	0.02	-1.60	12.6	1, 2
M3	15.02	0.01	-1.50	12.6	1
M5	14.46	0.03	-1.26	12.6	1, 2
M67	9.61	0.04	+0.00	3.5	3
NGC 6791	13.02	0.10	+0.40	10.0	4

Notes. ^a Adopted ages of clusters.

References. References for $(m - M)_0$, $E(B - V)$, and high-resolution spectroscopic $[\text{Fe}/\text{H}]$ values: (1) Kraft & Ivans 2003; (2) subdwarf-fitting distances from Carretta et al. (2000); (3) An et al. (2007b) and references therein; (4) D. An et al. (in preparation), and references therein.

To be consistent with our earlier color calibration with M67, we used the same color corrections as in An et al. (2009b). These are polynomial fits to the points over $4000 \leq T_{\text{eff}}(\text{K}) \leq 6000$,

Figure 3. Same as in Figure 1, but for $g - z$.Figure 4. Same as in Figure 1, but for $u - g$.

and are expressed as follows:

$$\Delta(g - r) = 7.610 - 19.910\theta + 17.279\theta^2 - 4.983\theta^3, \quad (1)$$

$$\Delta(g - i) = 6.541 - 16.313\theta + 13.461\theta^2 - 3.675\theta^3, \quad (2)$$

$$\Delta(g - z) = 3.755 - 7.595\theta + 4.535\theta^2 - 0.672\theta^3, \quad (3)$$

$$\Delta(u - g) = -7.923 + 24.131\theta - 23.727\theta^2 + 7.627\theta^3, \quad (4)$$

where $\theta \equiv T_{\text{eff}}/5040$ K. These corrections are shown as solid lines in Figures 1–4 (second panels from the bottom) and are in the sense that the above values should be added to the model colors. For M92, we used the color differences between the model and the cluster fiducial sequences as the baseline of the model calibration at the cluster’s metal abundance (see second panels from the top in Figures 1–4).

A quadratic relation in $[\text{Fe}/\text{H}]$ was then used to parameterize the metallicity dependence of the color–temperature corrections, assuming the following functional form:

$$\Delta_i(T_{\text{eff}}, [\text{Fe}/\text{H}]) = \delta_i(T_{\text{eff}}) + \zeta_i[\text{Fe}/\text{H}] + \xi_i[\text{Fe}/\text{H}]^2, \quad (5)$$

where Δ_i represents color corrections in each of $g - r$, $g - i$, $g - z$, or $u - g$, while δ_i represents color– T_{eff} corrections in Equations (1)–(4) in the i th color index at solar metallicity. Here, ζ_i and ξ_i are coefficients to be derived from the fit, where we used fiducial sequences for M15, M13, M3, M5, and NGC 6791. In fact, the problem is reduced to a single parameter fit, since our models were defined to match the observed main sequences of M67 and M92 at their metal abundances. The solid curves in Figures 1–4 show the resulting color corrections on the color– T_{eff} – $[\text{Fe}/\text{H}]$ space. We extrapolated color corrections below $[\text{Fe}/\text{H}] = -2.4$ using the best-fitting parameters obtained from the above equation.

The T_{eff} versus $[\text{Fe}/\text{H}]$ range covered by our calibrating sample clusters is sparse and non-uniform. In particular, hot stars ($T_{\text{eff}} \gtrsim 6000$ K) are not covered at or near solar abundance, while cool, metal-poor stars ($T_{\text{eff}} \lesssim 5000$ K) are outside of our calibration range. This is mainly because the clusters are found at varying distances from the Sun, while all of the cluster images were taken in drift-scan or time-delay-and-integrate (TDI) mode, with the same effective exposure time of 54.1 s per band. As a result, turnoff stars in M67 were too bright and lower main-sequence stars in M92 were too faint for SDSS to obtain

reliable magnitudes. The cluster age is an additional factor that affects the non-uniform coverage in the stellar parameter space.

In order to obtain full coverage of the color corrections in the T_{eff} versus $[\text{Fe}/\text{H}]$ plane, we assumed that the color difference from the model for M67/M92 at the high/low T_{eff} end extends and remains constant to $T_{\text{eff}} = 7000 \text{ K}/4000 \text{ K}$, respectively. We note that this reasonable, but arbitrary, extrapolation of the color– T_{eff} relations has minimal impact on the results of our analysis, because our calibrating cluster sample is in fact representative of the majority of stars detected in SDSS (in terms of T_{eff} and $[\text{Fe}/\text{H}]$, among other parameters). The purpose of the extrapolation is to obtain stable color– T_{eff} – $[\text{Fe}/\text{H}]$ relations going forward. Note that our model calibration is valid for main-sequence stars only.

Our adopted age of 13 Gyr at $-3.0 \leq [\text{Fe}/\text{H}] \leq -1.2$ in the color calibration (Section 2.1) is justified by our earlier result that the main-sequence turnoff ages of our calibrating clusters are approximately 13 Gyr, when pure theoretical YREC models are directly used in the age estimation (see Table 9 in An et al. 2009b). To a first approximation, a systematic error in the adopted age in the calibration results in a scale error in our color– T_{eff} corrections. Therefore, special attention should be paid when applying the models to stellar populations with different age–metallicity relations.

2.3. Stellar Parameter Search

We applied calibrated stellar isochrones to the observed *ugriz* magnitudes, and searched for the best-fitting stellar parameters— T_{eff} (or stellar mass), $[\text{Fe}/\text{H}]$, and an absolute magnitude (or distance)—by minimizing the χ^2 of the fit, defined as

$$\chi^2 = \sum_i \frac{(X_{\text{obs},i} - X_{\text{model},i})^2}{\sigma_i^2}, \quad (6)$$

for each star over $-3 \leq [\text{Fe}/\text{H}] \leq +0.4$. Here, $X_{\text{obs},i}$ and $X_{\text{model},i}$ are the observed and model magnitudes, respectively, in the i th bandpass. Stellar mass, $[\text{Fe}/\text{H}]$, and distances were set as free parameters (i.e., three parameters and five data points for each star). This is equivalent to fitting a model to the observed spectral energy distribution in the wavelength versus flux space.

We adopted foreground dust estimates by Schlegel et al. (1998), with theoretical extinction coefficients given by An et al. (2009b):

$$R_\lambda(\text{YREC}) = \frac{A_\lambda}{E(B - V)} = [4.858, 3.708, 2.709, 2.083, 1.513], \quad (7)$$

where $\lambda = u, g, r, i, z$, respectively. These extinction coefficients were computed using theoretical spectral energy distributions and the standard Cardelli et al. (1989) extinction curve. Our values are in good agreement with those provided in Girardi et al. (2004). The above values lie in between the default extinction coefficients in SDSS (Schlegel et al. 1998, SFD98) and those in Schlafly & Finkbeiner (2011, SF11):

$$R_\lambda(\text{SFD98}) = [5.155, 3.793, 2.751, 2.086, 1.479], \quad (8)$$

$$R_\lambda(\text{SF11}) = [4.239, 3.303, 2.285, 1.698, 1.263]. \quad (9)$$

In terms of the $u - g$ colors, which have a significant impact on photometric metallicity estimates, our $E(u - g) \equiv A_u - A_g$ coefficient is 18% smaller than the SFD98 value, but 19% larger than the Schlafly & Finkbeiner (2011) value. These differences are clearly important and we discuss their effect on our derived photometric MDFs in Section 4 below.

2.4. Comparisons with the SSPP Spectroscopic Estimates

Photometric temperatures and metallicities in our approach are derived simultaneously, based on the observed *ugriz* photometry. Each of these parameters are primarily constrained by different portions of the stellar spectral energy distribution; $u - g$ colors are mostly responsible for the photometric metallicities, while *griz* colors are sensitive to temperatures. Nevertheless, there is a moderate level of correlation between them, so checking a photometric temperature scale is an important step toward obtaining accurate photometric metal abundances of stars.

In Pinsonneault et al. (2012), we verified the accuracy of our photometric T_{eff} estimation procedure using the most recent temperature scale from the infrared flux method (IRFM) by Casagrande et al. (2010). Photometric temperatures were estimated from *griz* photometry in the *Kepler* Input Catalog (Brown et al. 2011) using a calibrated set of isochrones—the same set of models used in the current work—then they were compared to the IRFM temperatures derived from 2MASS $J - K_s$ colors. Overall, we found good agreement between these two fundamental temperature scales ($\langle \Delta T_{\text{eff}} \rangle \lesssim \pm 40 \text{ K}$) at $4400 \text{ K} < T_{\text{eff}} < 6000 \text{ K}$, where the IRFM scale is well defined; see Pinsonneault et al. (2012) for detailed discussions on this comparison.

Here we compare our photometric temperature estimates with the spectroscopic estimates obtained from medium-resolution SDSS/SEGUE spectra (Yanny et al. 2009); comparisons are shown in Figure 5. In this comparison, we included 51,999 stars from the initial sample of 162,645 objects that satisfy the following selection criteria:

1. Sources are detected in all five bandpasses.
2. $\chi_{\text{min}}^2/\nu < 3.0$, where χ_{min}^2 is a minimum χ^2 defined in Equation (6) and $\nu (= 2)$ is a degree of freedom.
3. $\sigma_u < 0.03 \text{ mag}$.
4. $\log g(\text{YREC}) \geq 4.15$.
5. $S/N(\text{SSPP}) > 20/1$.
6. $\log g(\text{SSPP}) \geq 3.5$.

where the subscripts YREC and SSPP indicate parameters estimated from the model isochrones and SSPP, respectively.

The first two criteria above require a good fit to the data, and the limit on the u -band measurement errors exclude data points with less well-defined photometric metallicity estimates. The $\log g$ limit restricts the analysis to main-sequence dwarfs. The last two criteria select dwarfs with reliable spectroscopic abundance measurements. We applied further cuts, based on colors ($g - r > 0.2$) and magnitudes ($r > 14 \text{ mag}$), in order to remove stars with extremely blue colors or saturated brightness measurements. Most of the stars in the original SSPP sample were rejected due to their large u -band errors. Even if a more conservative cut on $\chi_{\text{min}}^2/\nu < 10$ were used, there would still remain a total of 58,335 stars in the comparison.

As shown in Figure 5, there is a constant T_{eff} offset between the photometric and SSPP temperature scales over $5000 \text{ K} < T_{\text{eff}} < 6500 \text{ K}$, where the maximum deviation is less than 100 K in this temperature range. However, the good agreement between our temperature scale and the IRFM scale (Pinsonneault et al. 2012) ensures that our temperature estimates are more or less closer to the fundamental temperature scale.¹⁴ The random scatter seen in Figure 5 is $\sim 100 \text{ K}$ for individual T_{eff} estimates.

¹⁴ Further note that T_{eff} is a defined quantity in $L = 4\pi R^2 \sigma T_{\text{eff}}$.

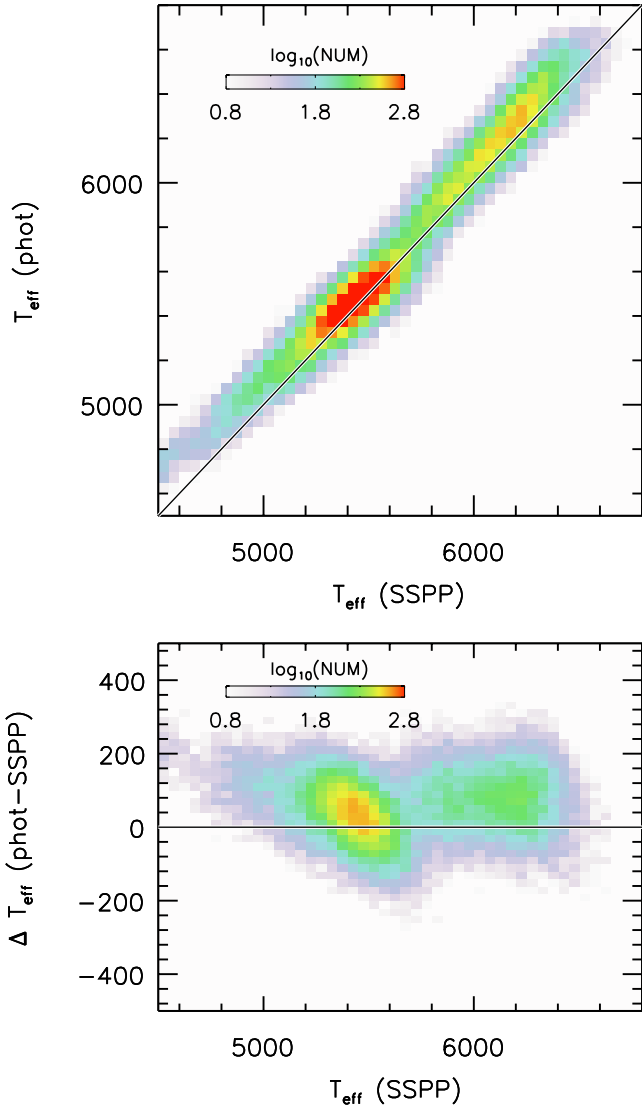


Figure 5. Comparison between photometric and spectroscopic (SSPP) temperature estimates for the SEGUE sample. The photometric estimates are based on all of the *ugriz* photometry.

(A color version of this figure is available in the online journal.)

Figure 6 shows a comparison between the spectroscopic (SSPP) metallicities from SDSS/SEGUE and our photometric estimates for the same set of stars, as in Figure 5. The central line in the top panel shows a median photometric metallicity for each 0.2 dex bin in the spectroscopic metallicity, and the other two lines represent the first and the third quartiles. An extended metal-poor tail at a given SSPP $[\text{Fe}/\text{H}]$ appears in Figure 6, in particular at low $[\text{Fe}/\text{H}]$ values. This is because the metallicity sensitivity of stellar colors degrades at lower metal abundances, due to the non-zero photometric errors. In the next section, we model these profiles based on simulations of artificial stars. As will be shown, artificial star tests indicate that the median photometric metallicities (central line in Figure 6) are insensitive to photometric errors and the lower limit in the model grid at $[\text{Fe}/\text{H}] = -3$ and exhibit a maximum deviation of only $\Delta[\text{Fe}/\text{H}] \sim 0.1$ dex from the true $[\text{Fe}/\text{H}]$ down to $[\text{Fe}/\text{H}] = -2.8$. The overall good agreement between our photometric metallicities and the SSPP values shown in Figure 6, with a maximum deviation of less than 0.2 dex, confirms that our photometric metallicity scale is not far from

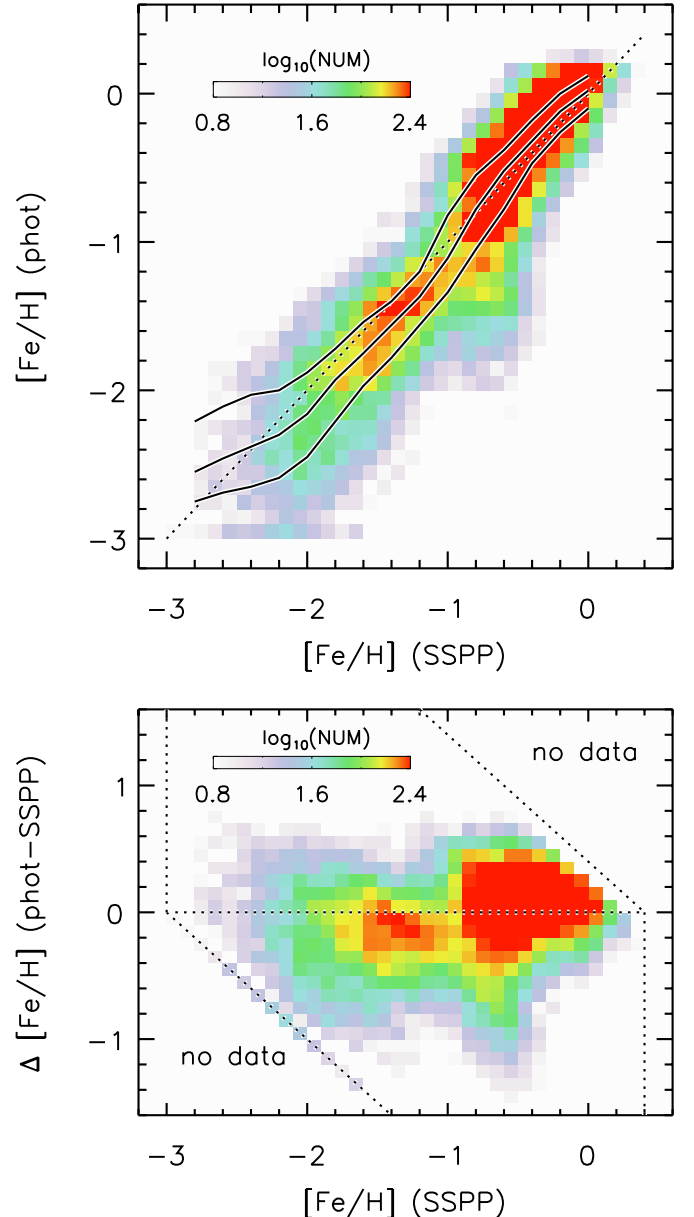


Figure 6. Comparison between photometric and spectroscopic (SSPP) metallicity estimates for the SEGUE sample. The photometric estimates are based on all of the *ugriz* photometry. Three curves in the top panel show a median and an interquartile range, respectively.

(A color version of this figure is available in the online journal.)

the spectroscopic scale down to $[\text{Fe}/\text{H}] \sim -2.5$, perhaps as low as ~ -3 . However, in order to perform a more stringent test of the accuracy of our photometric metallicity estimates, we require more comparison star samples below $[\text{Fe}/\text{H}] \sim -2.5$.

Because we included *u*-band measurements, which are more sensitive to metal abundances than the other SDSS bandpasses, the observed dispersion in Figure 6 is smaller than the equivalent Figure 2 in An et al. (2009a), which is based only upon *gri*. The 1σ random scatter (estimated from the interquartile range divided by 1.349, assuming a normal distribution) is about 0.2–0.4 dex for individual stars. The $[\text{Fe}/\text{H}]$ estimates in SDSS/SEGUE are precise to ~ 0.2 dex for individual stars (Lee et al. 2008a, 2008b; Allende Prieto et al. 2008; Smolinski et al. 2011), so this comparison indicates that the photometric metallicities can be as precise as ~ 0.3 dex per star, when good photometry is available. The downturn of the mean trend at $[\text{Fe}/\text{H}] \sim -0.8$

in Figure 6 is likely caused by our ad hoc assumptions on the $[\alpha/\text{Fe}]$ and age as a function of $[\text{Fe}/\text{H}]$ in the model.

An analysis of likely member stars of Galactic open and globular clusters and high-resolution spectra of SDSS/SEGUE stars indicates that the SSPP exhibits a tendency to estimate $[\text{Fe}/\text{H}]$ higher by about 0.25 dex for stars with $[\text{Fe}/\text{H}] < -3.0$, in particular for cool giants. Although the SSPP underestimates metallicities for stars with super solar abundances, the effect is less than 0.1 dex. Nevertheless, it should be kept in mind that the reliability of measuring photometric metallicities eventually requires a test against high-resolution spectroscopy.

In An et al. (2009a), we tested the accuracy of photometric metallicities from the application of *gri* photometry and found that the photometric technique systematically underestimates $[\text{Fe}/\text{H}]_{\text{phot}}$ in the low-metallicity range ($\Delta[\text{Fe}/\text{H}] \sim 0.3$ dex at $[\text{Fe}/\text{H}] \sim -1.6$). We speculated that the mismatch between the SSPP and photometric metallicities were likely caused by either unresolved binaries in the sample or a small zero-point offset in the model colors. Although the effect of unresolved binaries in the photometric metallicities cannot be completely ignored (see Section 2.5 below), small systematic color differences can actually induce a systematic trend in $[\text{Fe}/\text{H}]_{\text{phot}}$, especially when photometric metallicities are derived based on color indices that are weakly dependent on $[\text{Fe}/\text{H}]$, such as the application of *gri* photometry in An et al. (2009a). The accuracy of the photometric technique (Figure 6) has improved as more metallicity-sensitive color indices (*ugriz*) are employed in the calculation of $[\text{Fe}/\text{H}]_{\text{phot}}$.

Figure 7 is the same as Figures 5 and 6, but based only on *ugr* colors. The scatter in the comparison is larger than those seen in Figures 5 and 6, because of the weaker constraints on these parameters. The downturn of the mean trend at $[\text{Fe}/\text{H}] \sim -0.8$ is stronger than seen in Figure 6. Clearly, the inclusion of all *ugriz* passbands is preferred, in order to strongly constrain both photometric temperatures and metal abundances.

2.5. Artificial Star Tests

We performed artificial star tests in order to evaluate the effects of photometric errors and unresolved binaries and/or blends on our determinations of photometric $[\text{Fe}/\text{H}]$ estimates. In particular, we use these simulation results to construct metallicity kernels, which are employed to assess the broadening of the $[\text{Fe}/\text{H}]$ profiles resulting from the above effects. These kernels are then used in Section 4 to deconvolve the observed MDF of the halo.

Figure 8 shows the artificial star test results for a single stellar population without binaries. In this exercise, we used the same set of models as in Section 2.2, which include the main sequence and a portion of the subgiant branch. For each of the various metallicity bins, we generated 20,000 artificial stars with masses above $0.65 M_{\odot}$ from a model isochrone. The magnitudes were then convolved with a Gaussian having a standard deviation of 0.02 mag in *gri*, and 0.03 mag in the *u* and *z* passbands. We derived photometric metallicities and distance estimates as described in Section 2.3; the resulting MDFs are shown as solid black histograms in the left panels, and the distributions in distance modulus are in the right panels. We used the following selection criteria.

1. $\chi_{\text{min}}^2/\nu < 3.0$, where χ_{min}^2 is a minimum χ^2 defined in Equation (6) and ν ($= 2$) is a degree of freedom.
2. $\log g(\text{YREC}) \geq 4.15$.
3. $0.65 < M_*/M_{\text{sun}} < 0.75$.

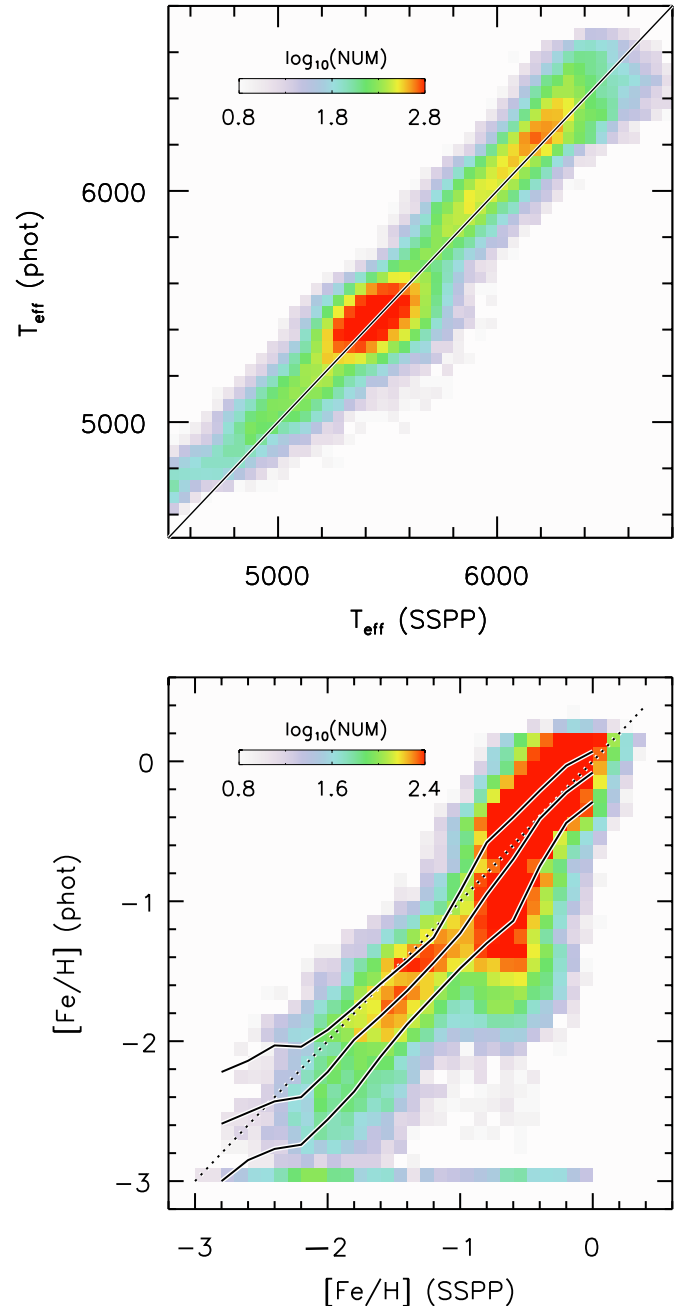


Figure 7. Comparisons between photometric and spectroscopic (SSPP) temperature (top panel) and metallicity estimates (bottom panel) for the SEGUE sample. Photometric estimates are based only on *ugr* photometry. Three curves in the bottom panel show a median and an interquartile range, respectively.

(A color version of this figure is available in the online journal.)

The last criterion is specified in order to be consistent with the analysis of the actual data sets described in Section 4 and assumes that stars are on the main sequence.

The solid red histograms shown in Figure 8 are those resulting from the simulations, but assuming photometric errors twice the size as above (0.04 mag error in *gri*, 0.06 mag error in *u* and *z*, and assuming no correlation between the errors in different bandpasses), illustrating the effect of the size of photometric errors on the photometric metallicity estimates. For a given photometric error, the resulting dispersion is higher at lower metallicity, due to the weaker dependence of broadband photometric colors on metallicity at lower abundances, e.g., see Figure 1 in An et al. (2009a). At solar abundance, the

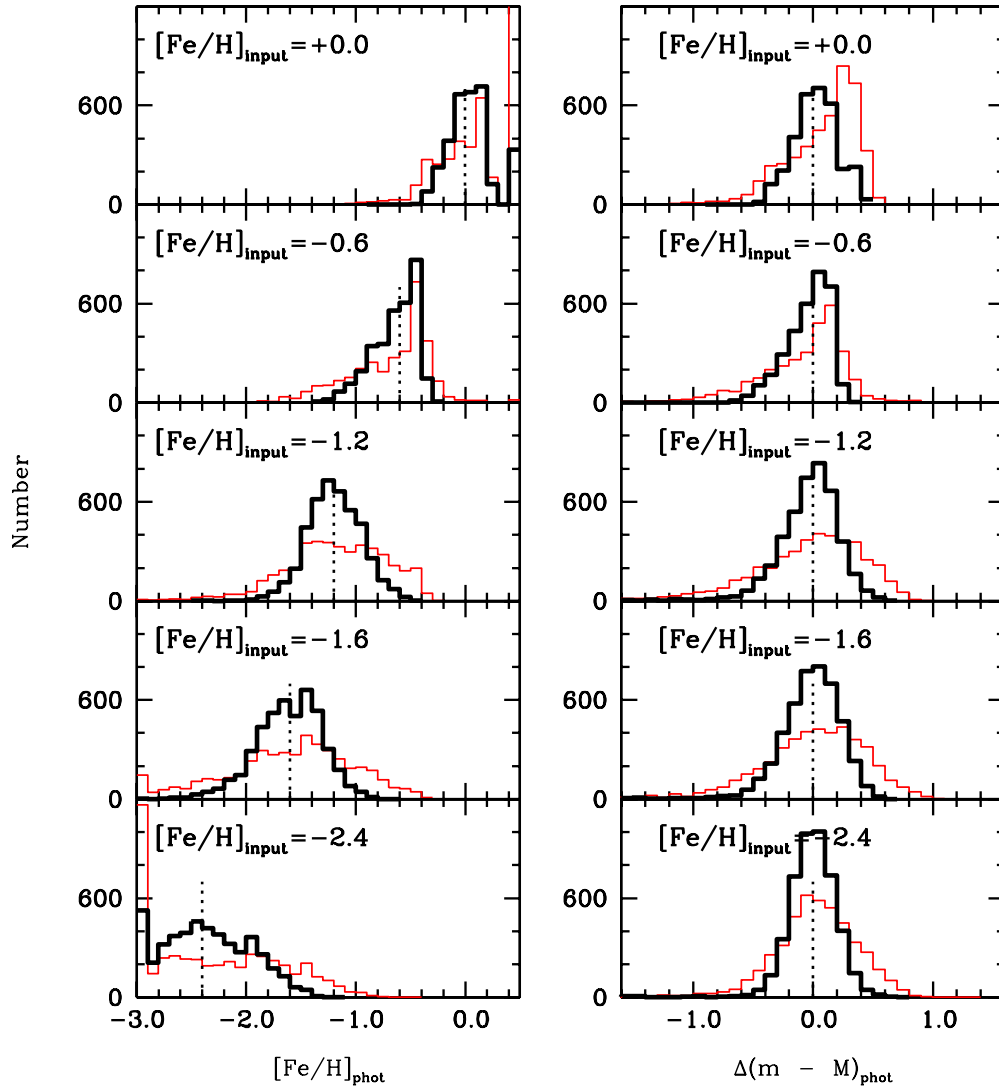


Figure 8. Artificial star tests for various metallicity bins. Left: the thick black histogram shows a photometric MDF, where photometric errors of 0.02 mag in *gri* and 0.03 mag in *u* and *z* passbands were assumed. The thin red histograms show the case when photometric errors are twice the size of these errors. Input $[\text{Fe}/\text{H}]_{\text{input}}$ values are shown on each panel and indicated by the dotted vertical lines. No binaries are included in the simulation. Right: same as in the left panels, but for the displacement in distance modulus.

(A color version of this figure is available in the online journal.)

standard deviation of the $[\text{Fe}/\text{H}]$ distribution in Figure 8 is 0.1 dex, but increases to 0.3 dex at $[\text{Fe}/\text{H}] = -1.6$ and 0.5 dex at $[\text{Fe}/\text{H}] = -2.4$. At the lowest $[\text{Fe}/\text{H}]$, the distribution becomes asymmetric, with an extended low-metallicity tail. On the other hand, the distribution in distance modulus becomes progressively more symmetric at the lower input metallicity, because of the weaker metallicity sensitivity of colors and magnitudes at lower metal abundances. Our model set does not extend below $[\text{Fe}/\text{H}] = -3$ or above $[\text{Fe}/\text{H}] = +0.4$, which results in a piling up of stars at these metallicities.

Figure 9 shows the effects of unresolved binaries and/or blends for three metallicity bins, $[\text{Fe}/\text{H}]_{\text{input}} = -1.6$ (left panels), -2.0 (middle panels), and -2.4 (right panels), respectively. Photometric errors of 0.02 mag in *gri* and 0.03 mag in *u* and *z* passbands were assumed. To reduce the effects of interpolation errors in the isochrones, which sometimes produce a non-continuous distribution in $[\text{Fe}/\text{H}]_{\text{phot}}$, we convolved the derived photometric metallicities with Gaussians having the grid size of the model ($\sigma_{[\text{Fe}/\text{H}]} = 0.1$ dex). The top panels apply to stellar populations comprised entirely of single stars. The middle two

panels show the results when unresolved binaries are included in the sample. In total, 10,000 primary stars were generated from a single $[\text{Fe}/\text{H}]$ population, and the same number of secondary stars was generated, based either on a flat mass function, or adopting the M35 mass function (Barrado y Navascués et al. 2001). These simulated stars were merged with 10,000 single stars with no secondary components to simulate a 50% unresolved binary fraction. The resulting magnitudes in *ugriz* were convolved with Gaussians having the specified photometric errors.

As can be appreciated by inspection of Figure 9, the presence of unresolved binaries has little impact on the derived photometric $[\text{Fe}/\text{H}]$ distribution, because the dispersion is dominated by the effects of photometric errors. Binaries, due to the modified flux distributions due to a secondary component, typically have lower photometric metal abundances than those of the primaries alone, but these effects are mostly buried in the extended $[\text{Fe}/\text{H}]$ distribution produced by the presence of non-zero photometric errors. The bottom panels in Figure 9 show photometric metallicity distributions of the SDSS/SEGUE spectroscopic

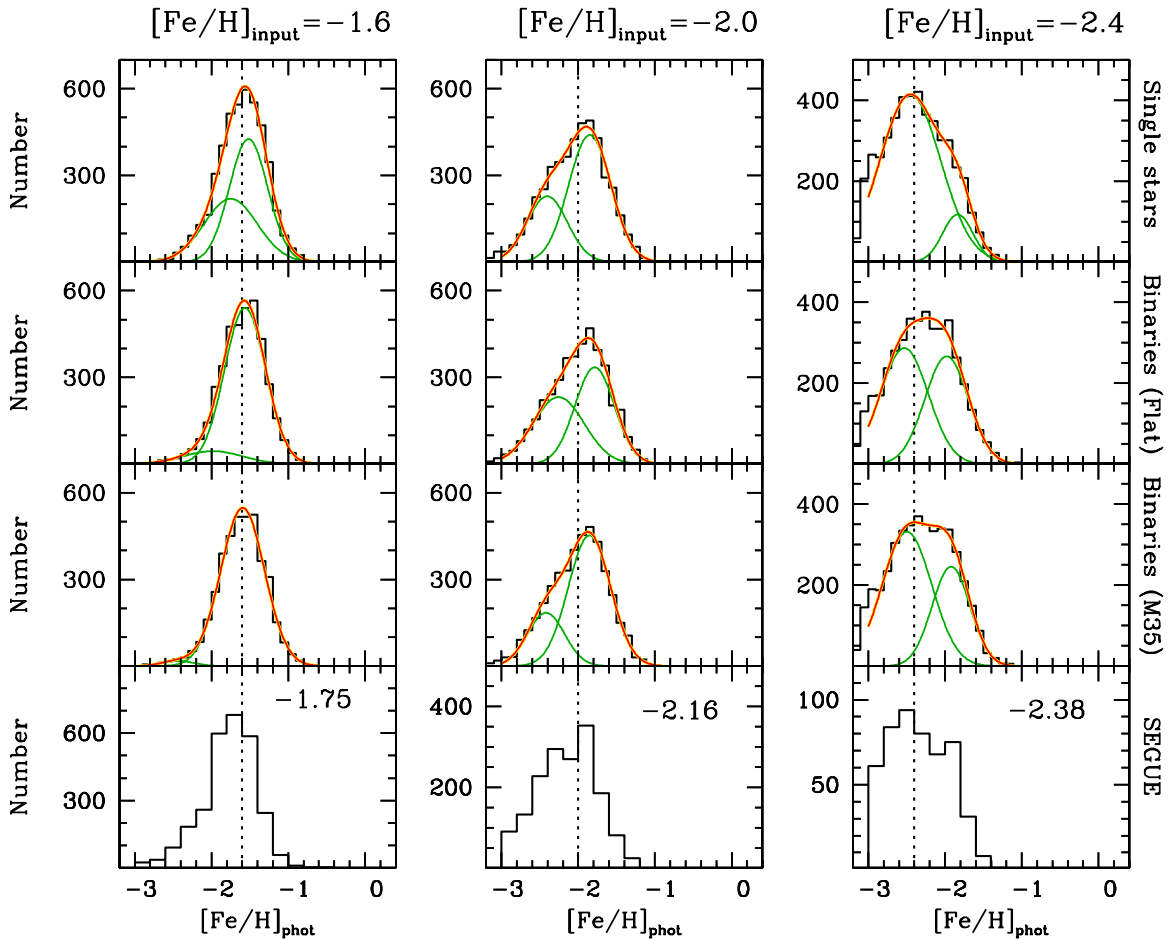


Figure 9. Effects of unresolved binaries and/or blends from artificial star tests at three input metallicity bins: $[\text{Fe}/\text{H}]_{\text{input}} = -1.6$ (left), -2.0 (middle), and -2.4 (right). Top: a single star population without binaries. Middle: a 50% unresolved binary fraction with a flat, and a M35-type mass function, respectively, for secondaries. The green curves in each panel show Gaussian fits to the distribution; the red curve is their sum. Bottom: photometric metallicity distributions of SDSS/SEGUE spectroscopic samples in the same metallicity ranges: $-1.7 \leq [\text{Fe}/\text{H}]_{\text{SSPP}} < -1.5$ (left), $-2.1 \leq [\text{Fe}/\text{H}]_{\text{SSPP}} < -1.9$ (middle), $-2.5 \leq [\text{Fe}/\text{H}]_{\text{SSPP}} < -2.3$ (right). Median $[\text{Fe}/\text{H}]_{\text{phot}}$ values are shown in the panels.

(A color version of this figure is available in the online journal.)

sample in Figures 5 and 6 in the same metallicity bins: $-1.7 \leq [\text{Fe}/\text{H}]_{\text{SSPP}} < -1.5$ (bottom left), $-2.1 \leq [\text{Fe}/\text{H}]_{\text{SSPP}} < -1.9$ (bottom middle), $-2.5 \leq [\text{Fe}/\text{H}]_{\text{SSPP}} < -2.3$ (bottom right). Except for a small offset in the metallicity scale between the SSPP and photometric metallicities (median $[\text{Fe}/\text{H}]_{\text{phot}}$ values are shown in the panels), which has already been pointed out in Section 2.4, the overall $[\text{Fe}/\text{H}]_{\text{phot}}$ distributions appear quite similar to those from the artificial star tests.

Our strategy in this study is to deconvolve the observed MDF of halo stars using simulated profiles and infer the underlying $[\text{Fe}/\text{H}]$ distribution (Section 4). In order to carry out the deconvolution in a straightforward manner, we parameterized simulated $[\text{Fe}/\text{H}]$ kernels by simultaneously fitting two Gaussian functions, as shown by the two green curves in each panel of Figure 9. The red curve is a sum of these two distributions. As discussed above, the precise binary fractions and the exact form of the adopted mass functions are not dominant factors in determining the overall shape of a given MDF. Therefore, we opted to choose the M35 mass function with a 50% binary and/or blending fraction when comparing the observed MDF of the halo with simulated results.

The top panel in Figure 10 displays photometric metallicity kernels for various input metallicity values ($[\text{Fe}/\text{H}]_{\text{input}}$), normalized to the peak value of each profile. These simulated profiles were generated from the same set of artificial star tests

as above, assuming a M35-type mass function and by taking 0.02 mag error in gri and 0.03 mag error in u and z . The input $[\text{Fe}/\text{H}]_{\text{input}}$ values are from -1.2 to -2.8 in intervals of 0.1 dex; for clarity, the simulated profiles are alternatively shown in thick and thin curves. Again, note that the resulting photometric distribution becomes broader at lower metallicities.

The bottom panel in Figure 10 shows the median differences between photometric metallicities and input $[\text{Fe}/\text{H}]$ values for the same data set used to construct the kernels in the top panel. Longer error bars represent the interquartile ranges, while the shorter error bars represent $\pm 1\sigma$ errors, where we computed the 1σ error by dividing the interquartile ranges by 1.349, assuming a normal distribution.

3. SAMPLE SELECTION AND PROPERTIES

Using the new photometric metallicity estimation technique described in the previous section, we estimated distances and metal abundances for individual stars in SDSS Stripe 82, which is one of the imaging stripes in SDSS that has been repeatedly scanned along the celestial equator. There are two photometric catalogs available in Stripe 82: the *calibration* or Standard Star catalog (Ivezić et al. 2007, hereafter calibration catalog)¹⁵ and

¹⁵ Available at <http://www.astro.washington.edu/users/ivezic/sdss/catalogs/stripe82.html>.

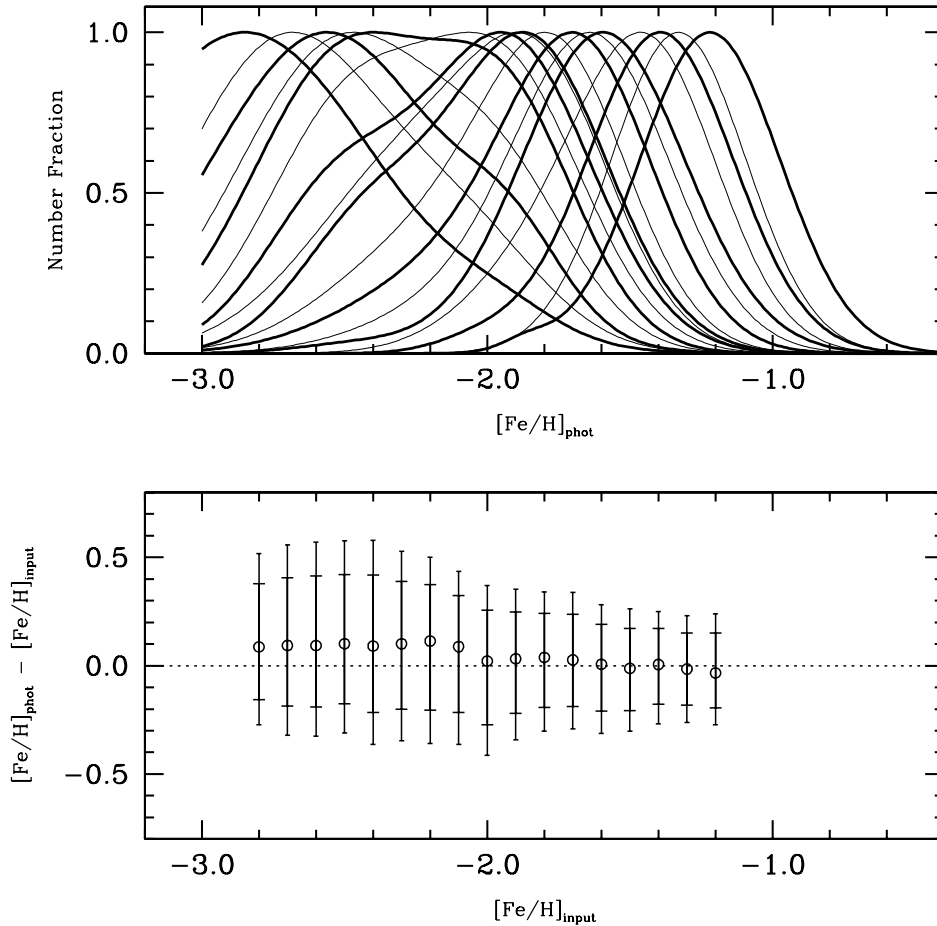


Figure 10. Top: normalized distributions of photometric metallicities at various input $[\text{Fe}/\text{H}]_{\text{input}}$ values. These simulated profiles were generated from artificial star tests at a given input $[\text{Fe}/\text{H}]_{\text{input}}$, assuming a 50% binary fraction and a M35-type mass function, and by taking 0.02–0.03 mag errors in *ugriz* (see the text). Input $[\text{Fe}/\text{H}]$ values are from -2.8 to -1.2 in an 0.1 dex increment, where simulated profiles are shown alternatively in thick and thin curves. Bottom: median differences between photometric metallicities and input values. Longer error bars show interquartile ranges, and the shorter error bars represent $\pm 1\sigma$ errors. The latter values were computed from the interquartile ranges divided by 1.349.

the *co-add* imaging catalog (Annis et al. 2011, hereafter *co-added* catalog). The calibration star catalog contains stellar magnitudes for approximately one million sources, where the magnitudes were averaged at the catalog level. The *co-added* catalog is based on the *co-added* image products and is about 0.5 mag deeper than the calibration catalog. Both catalogs, which were in principle produced from the same observations, obtained with the ARC 2.5 m SDSS survey telescope facilities, provide the most precise ($\sim 1\%$) photometry set available within SDSS, and therefore can be used to set the best available constraints on the photometric MDF of the Galaxy. Both catalogs were constructed on the Photo magnitude system. However, we directly employed our UberCal-based models in the parameter estimation using this photometry, because the global photometric zero-point differences between the two systems are negligible.

Below, we describe the selection of a photometric sample from Stripe 82 designed to minimize bias (Section 3.1) and evaluate the effects of unrecognized giants in the sample (Section 3.2). In the subsequent section (Section 4), we present an unbiased MDF of the Galactic halo, and test the hypothesis that the halo is composed of two overlapping sub-components, based on both metallicity and kinematic information for our sample stars.

3.1. Sample Selection and Bias

An unbiased sample of stars is, of course, an important ingredient for obtaining a representative MDF of the Milky Way’s halo population(s). Although photometric samples are less susceptible to sample biases than spectroscopic studies that make use of metallicity or color in their sample selection, a bias still exists that needs to be taken into account, as discussed below.

In this work we adopted a sample selection based on stellar mass, as estimated using our isochrones. Figure 11 shows our color-calibrated models at $[\text{Fe}/\text{H}] = -2.4, -1.6, -1.2,$ and -0.8 ; the thick solid lines indicate where $0.65 < M_*/M_\odot < 0.75$. This range of stellar mass is similar to what is adopted in this work (see below). Our choice for the mass-based sample selection was motivated by our reasoning that, in order to obtain a representative sample of the halo, stars at different metallicities should be sampled in identical mass ranges. We consider this to be a superior choice to the more commonly adopted color-based selections, because of the strong relationship between color, metallicity, and mass; narrow color cuts in a stellar sample would produce a mix of stars, including less massive, lower metallicity stars and more massive, higher metallicity stars. Although colors can be used as a surrogate for temperatures, they have only a

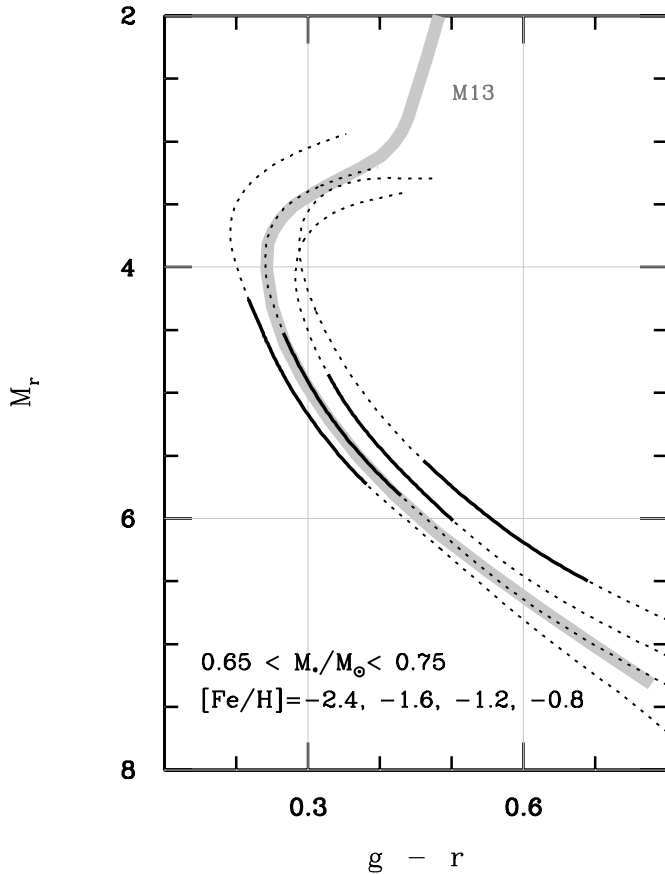


Figure 11. Range of stellar mass in the model considered in this work. Color-calibrated models are shown at $[\text{Fe}/\text{H}] = -2.4$ (13 Gyr; leftmost), -1.6 (13 Gyr), -1.2 (13 Gyr), and -0.8 (9 Gyr; rightmost), where solid lines represent $0.65 < M_*/M_\odot < 0.75$. The fiducial sequence of M13 is shown as a gray line for comparison.

limited applicability for stellar masses, hence we believe our mass-based selection should produce a less biased sample of stars for the assembly of a valid halo MDF.

Figure 12 illustrates metallicity–luminosity relations as a function of stellar mass, where the luminosity is expressed in terms of a maximum heliocentric distance that can be reached by a star at a specific magnitude limit. Note that we adopted an age of 13 Gyr for models at $-3.0 \leq [\text{Fe}/\text{H}] \leq -1.2$, and 4 Gyr at $-0.3 \leq [\text{Fe}/\text{H}] \leq +0.4$, with a linear interpolation between these two metallicity ranges (Section 2.1). The u -band magnitude limit was used in Figure 12, because of the strong sensitivity of this band on metal abundances. The $u_{\text{max}} = 20.6$ (top panel) and $u_{\text{max}} = 21.0$ (bottom panel) correspond to a median photometry error of $\sigma \approx 0.03$ mag in the calibration and the co-added catalogs, respectively. The error size is similar to those adopted in the artificial star tests (Section 2.5).

At a given u -band magnitude limit, we computed a maximum distance to which each star can be observed at a given stellar mass and metal abundance. At a fixed mass, metal-poor stars are brighter than metal-rich stars, thus they can be observed at greater distances than metal-rich stars (see Figure 11). Note that a color-based selection would have the opposite consequence on the luminosity of stars that would be included; at a fixed color (or temperature) stars are brighter at higher metallicity. It follows that, in a magnitude-limited survey such as SDSS, color-based selection would produce samples that are biased against more metal-poor stars at greater distances from the Sun.

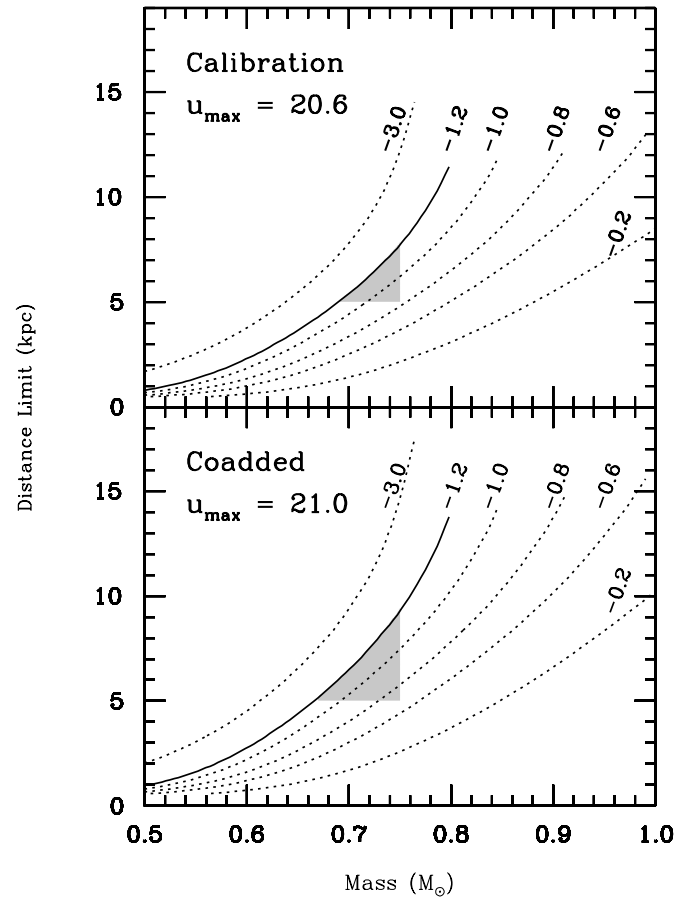


Figure 12. Maximum heliocentric distance as a function of stellar mass that can be reached by a star at $u < 20.6$ mag (top panel) and $u < 21.0$ mag (bottom panel). These magnitude limits correspond to $\sigma_u \approx 0.03$ mag error in u in the Stripe 82 calibration (top) and co-added (bottom) catalogs, respectively. The solid and dotted curves show distance limits at a number of different metallicity bins. The gray shaded region represents a mass–distance limit set for the halo sample in this work, which ensures that the sample is unbiased at $[\text{Fe}/\text{H}] \lesssim -1.2$, has a stellar mass less than the turnoff mass of the $[\text{Fe}/\text{H}] = -3$ model, and is relatively free from thick-disk contamination ($d_{\text{helio}} > 5$ kpc).

The gray shaded region in Figure 12 indicates the mass–distance limit set in our halo sample. In both panels, these areas are surrounded by an $[\text{Fe}/\text{H}] = -1.2$ model to insure that the sample is unbiased at $[\text{Fe}/\text{H}] \leq -1.2$. Our photometric halo MDFs should be less affected by this choice, since we generally expect to obtain relatively few halo stars outside this metallicity range. An additional constraint on the stellar mass has been applied to the sample, because main-sequence turnoff masses (the high-mass end points of each curve in Figure 12) are varying at different metallicities. Therefore, we imposed an upper mass limit, $M_* < 0.75 M_\odot$, which is close to the main-sequence turnoff mass from an $[\text{Fe}/\text{H}] = -3$ model; turnoff masses occur at higher masses for $[\text{Fe}/\text{H}] > -3$. The lower limit to the heliocentric distance (5 kpc) was set to exclude possible thick-disk interlopers in the sample; this naturally results in a lower mass cut-off at $\sim 0.65 M_\odot$. We further imposed a cut based on Galactic latitude (see discussion below in Section 4.1). The application of these constraints results in a relatively narrow parameter space (gray areas in Figure 12) in the stellar mass versus distance plane ($5 \text{ kpc} \leq d_{\text{helio}} \lesssim 8 \text{ kpc}$ for the calibration catalog; $5 \text{ kpc} \leq d_{\text{helio}} \lesssim 9 \text{ kpc}$ for the co-added catalog). In short, our sample selection (delineated by the gray regions in Figure 12) collects all of the stars at $[\text{Fe}/\text{H}] \lesssim -1.2$ in a

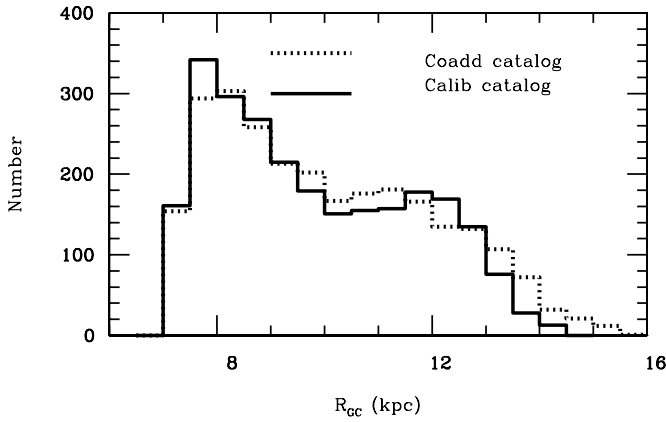


Figure 13. Distribution of Galactocentric distances for the final halo samples in the calibration and the co-added catalogs in Stripe 82.

limited volume of the halo, given the magnitude limit set in a photometric catalog ($\sigma_u < 0.03$ mag in this work). The resulting distribution of our sample in Galactocentric distances is shown in Figure 13.

We have carried out comparisons of our samples obtained by both the calibration and the co-added catalogs, using a search radius of $1''$. As recommended in Ivezić et al. (2007), we only included sources in the calibration catalog with at least four repeated observations in each bandpass, for both the photometric comparisons and the following analysis, and proceed with the mean magnitudes and their standard errors. After carrying out iterative 3σ rejections, we found zero-point differences of -0.007 ± 0.022 mag, -0.001 ± 0.011 mag, $+0.002 \pm 0.013$ mag, and $+0.003 \pm 0.015$ mag, in $u - g$, $g - r$, $g - i$, and $g - z$, respectively, for stars with $u < 20.6$ and fainter than 16th magnitude in each filter bandpass; see also photometric comparisons in Annis et al. (2011). The sense of these differences is that the $u - g$ color measurements in the co-added catalog are redder than those in the calibration catalog. We restricted our comparison to only include those stars with Galactic latitudes at $|b| > 35^\circ$, to be consistent with the analysis of the halo MDF carried out below. The listed errors indicate the derived dispersions in color difference (rather than the errors in the mean), using $\sim 100,000$ objects in each comparison. Because fainter u -band measurements yield less strong UV excesses, the use of photometry from the co-added catalog would lead to systematically higher photometric metallicity estimates than in the calibration catalog (this is confirmed in the next section). The rms deviations of the color differences between the two catalogs are stable ($\sigma_{\text{color}} < 0.003$ mag) along the 110° length of Stripe 82.

Although a detailed study is beyond the scope of the present work, we identified a strong systematic deviation in the u passband ($\Delta u \sim 0.2$ mag at $u \sim 22$ mag) at the faint end, beyond the magnitude limit set in our sample ($u < 20.6$). One likely cause of the systematic offset is a Malmquist-type bias in the calibration catalog, because faint sources near the detection limit can either be detected or missed, due to the existence of large Poisson errors. Since the calibration catalog took the average of the source magnitudes from individual images, the mean magnitude could therefore be biased toward brighter source measurements. We avoided the photometry zero-point issue by requiring $\sigma_u < 0.03$ mag; small photometric errors also make the photometric metallicity estimates more reliable.

We have not made use of the main SDSS photometric database in this work. The 95% completeness limit in the u bandpass of

the main survey is 22.0 mag, but the $\sigma_u = 0.03$ mag limit corresponds to $u \approx 18.7$ mag, on the order of 2 mag shallower than for the Stripe 82 catalog. At this limiting magnitude, use of the main SDSS database would allow exploration of heliocentric distances only up to ~ 2.2 kpc for the construction of an unbiased $[\text{Fe}/\text{H}]$ sample at $[\text{Fe}/\text{H}] < -1.2$, which is an insufficient volume to probe the halo MDF.

To summarize, in the following analysis we used the selection criteria listed below.

1. Sources are detected in all five bandpasses.
2. $\chi_{\text{min}}^2/\nu < 3.0$, where χ_{min}^2 is a minimum χ^2 defined in Equation (6) and ν ($= 2$) is a degree of freedom.
3. $\log g_{(\text{YREC})} \geq 4.15$.
4. $0.65 M_\odot < M_* < 0.75 M_\odot$.
5. Mass–metallicity–luminosity limits (gray region in Figure 12).
6. $d_{\text{helio}} > 5$ kpc.
7. $|b| > 35^\circ$.

The above selection restricts the photometric sample to $0.2 \lesssim g - r \lesssim 0.5$ (see Figure 11). The total numbers of objects that passed the above selection criteria are 2523 from the calibration catalog and 2626 from the co-added catalog. The median r magnitudes are 18.7 mag and 19.1 mag for the calibration and the co-added catalogs, respectively, with a ~ 0.3 mag dispersion. The standard SDSS star–galaxy separation based on the difference between point-spread function (PSF) and model magnitudes is robust to $r \sim 21.5$ (Lupton et al. 2002; Scranton et al. 2002), so the contamination by galaxies in our sample should be negligible (see also Annis et al. 2011; Bovy et al. 2012a).

3.2. Contamination by Distant Giants and Thick Disk Stars

Our calibration is valid for main-sequence stars only, and we have explicitly assumed that the great majority of stars in the sample are in their main-sequence phase of evolution. However, there certainly exist distant background giants and subgiants along each line of sight, and their distances can be greatly underestimated if a photometric parallax relation for main-sequence stars is blindly applied. Unfortunately, $ugriz$ photometry alone is not sufficient to reliably discriminate giants from dwarfs, unlike horizontal-branch stars (Ivezić et al. 2007), and therefore some level of contamination by giants in our sample is unavoidable.

We evaluated the level of expected giant and subgiant contamination using cluster photometry for both M13 ($[\text{Fe}/\text{H}] = -1.6$; see Figure 11) and M92 ($[\text{Fe}/\text{H}] = -2.4$) (An et al. 2008). In order to carry this out, we applied cuts based on χ and sharp parameters in DAOPHOT (Stetson 1987) as in An et al. (2008). Based on the large extent of these clusters on the SDSS CCD chips, we opted not to apply cuts based on the distance from the cluster centers.

We assumed that the number density of the halo follows a power-law profile with an index of -2.8 and a halo ellipticity of 0.6 (e.g., Jurić et al. 2008). Using this model, along with the photometry for each cluster, we simulated color–magnitude diagrams for each line of sight in Stripe 82, and applied the same mass–metallicity–luminosity cuts to the sample as in the previous section. We integrated the number of giants out to 30 kpc from the Sun, beyond which the giant contamination is negligible, because either those distant giants are too faint to be included in our sample or they do not satisfy our selection criteria. Each object was tagged as either a (sub)giant

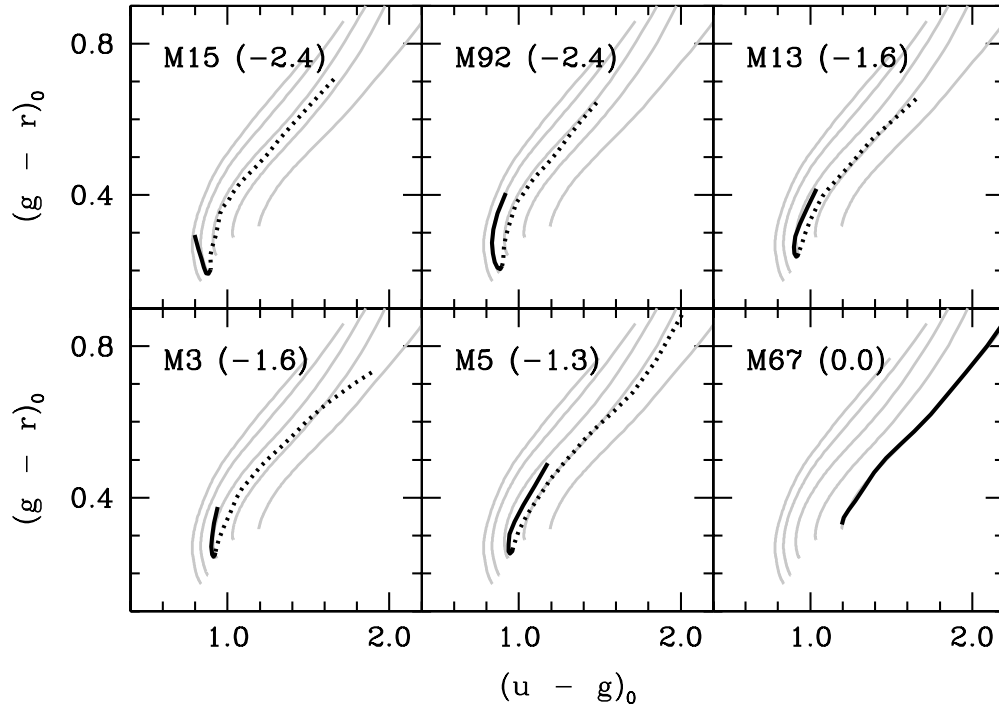


Figure 14. Fiducial sequences of the calibration cluster sample (black lines) in the $u - g$ vs. $g - r$ plane. The solid black lines represent a dwarf sequence; dotted lines show the giant sequence. Overlaid gray lines are calibrated models at $[\text{Fe}/\text{H}] = -3.0$ (left), -2.4 , -1.6 , -0.8 , and 0.0 (right), respectively. At a given $g - r$, giants have redder $u - g$ colors than the main sequence, leading to an overestimated photometric metallicity. Values in parentheses next to the cluster name indicate the cluster metal abundance in $[\text{Fe}/\text{H}]$.

or a dwarf, depending on the location on the original cluster color–magnitude diagram, and the number of giants included in the sample was counted. From the above calculation we found that the contamination rates are at about the 10%–15% level from the M13 photometry, and the 15%–20% level when using the M92 photometry. M92 is more metal-poor than M13, so more cluster giants fall in the color range ($0.2 \lesssim g - r \lesssim 0.5$), which is implicitly set by our sample selection criteria. This results in a slightly higher contamination rate from the M92 photometry.

More than any other parameters (e.g., shape parameters of the halo) in the model, we found that the assumed fraction of giants is the dominating factor that determines the total contamination rate in our sample. Note that our estimate for giant contamination in the sample is higher than what Jurić et al. (2008) estimated ($\sim 15\%$ versus $\sim 4\%$). Jurić et al. (2008) obtained an estimate of the fraction of giants to be about 5% from M13, using the SDSS pipeline *Photo* values in this crowded region, over a color range similar to that in our analysis, and concluded that the bias in the number density of the halo is about 4% arising from the misidentification of giants as main-sequence dwarfs.

Giant contamination in our sample produces an overall shift of the photometric metallicity estimates toward higher values. Figure 14 shows the fiducial sequences on the $u - g$ versus $g - r$ diagram for a number of clusters that were used in our color calibration. The black lines shown are fiducial sequences, with the dotted lines indicating a giant sequence. For M67, only a main sequence was detected in SDSS (giants are too bright to be included; An et al. 2008). The overlaid gray lines in each panel show our calibrated models at $[\text{Fe}/\text{H}] = -3.0$ (left most), -2.4 , -1.6 , -0.8 , and 0.0 (right most), respectively. At a given $g - r$, giants have redder $u - g$ colors than the main sequence, which leads to an overestimated photometric metallicity if they are misidentified as dwarfs. The size of a bias in the photometric

metallicity can be as large as 0.5–1 dex, but fortunately this only applies for a limited number of stars along each line of sight.

On the other hand, contamination by thick-disk stars in our sample is negligible. We performed a set of Galactic simulations to check the overall fraction of thick-disk interlopers in our sample along various lines of sight, using artificial star test results in Section 2.5. To simulate a dispersion in the underlying $[\text{Fe}/\text{H}]$ distribution, we combined artificial stars at the central $[\text{Fe}/\text{H}]$ (≈ -0.7 for the thick disk and ≈ -1.6 for the halo) with those at $\pm 1\sigma$ values (± 0.2 and ± 0.4 dex for the thick disk and the halo, respectively), taking normalizations from a Gaussian distribution. We adopted the Galactic structural parameters in Jurić et al. (2008).

The fraction of thick-disk stars, of course, is varying at different Galactic latitudes, so we computed the fraction of thick-disk stars along Stripe 82. We found that the average fraction is negligible (0.4% of the entire sample) below photometric $[\text{Fe}/\text{H}] = -1.0$ (see also Bovy et al. 2012b). This is because our sample selection, based on mass, metallicity, and distance, is strongly biased against stars with $[\text{Fe}/\text{H}] > -1.2$. If all the stars below solar metallicity are included in this estimate, the fraction becomes $\sim 3.4\%$. However, only stars with photometric metallicities less than $[\text{Fe}/\text{H}] = -1$ are concerned in the following discussions, and we can safely assume that the thick-disk contamination is negligible.

4. RESULTS

4.1. The Observed Metallicity Distribution Function of the Galactic Halo

Figure 15 shows our in situ observed MDFs from the calibration (top panel) and the co-added catalogs (bottom panel), respectively, including only stars satisfying the selection criteria described above. Jurić et al. (2008) found that both thick-disk

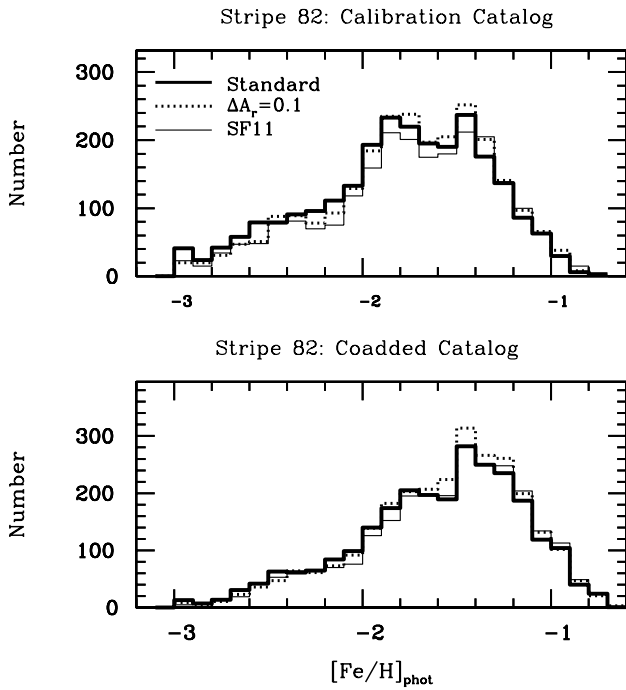


Figure 15. Photometric MDFs of the halo. The black solid histogram shows an MDF using our adopted extinctions and extinction coefficients. The dotted histogram is an MDF assuming 10% smaller extinction values; the thin solid histogram represents a case assuming extinction coefficients from Schlafly & Finkbeiner (2011). The top panel shows the MDF from the calibration catalog and the bottom panel shows the MDF from the co-added catalog. The photometric MDFs are complete for $[\text{Fe}/\text{H}]_{\text{true}} \leq -1.2$.

and halo stars have approximately the same number density at 3 kpc above the Galactic plane. In order to minimize the contribution from thick-disk interlopers in our halo sample, we imposed a heliocentric distance limit of greater than 5 kpc and Galactic latitudes $|b| > 35^\circ$, which correspond to a minimum vertical distance $|Z| = 2.9$ kpc from the Galactic plane at the low-latitude limit. As noted above, we imposed a sample cut at $[\text{Fe}/\text{H}]_{\text{true}} = -1.2$, where $[\text{Fe}/\text{H}]_{\text{true}}$ indicates a true metallicity value. The great majority of thick-disk stars having metallicities above this limit would have been excluded from our photometric sample selection. Nevertheless, it remains possible that some metal-weak thick-disk stars (Chiba & Beers 2000; Carollo et al. 2010, and references therein) have entered our sample, at least near the low-latitude limit. Note that some stars near $[\text{Fe}/\text{H}]_{\text{true}} = -1.2$ could have photometric metallicities greater than $[\text{Fe}/\text{H}]_{\text{phot}} = -1.2$, because of non-zero photometric errors.

The thick solid histograms in Figure 15 show our derived photometric MDFs, constructed using the YREC-based extinction coefficients in Section 2.3; the dotted lines represent the case with 10% smaller extinction values than in Schlegel et al. (1998). The thin solid histograms are those based on extinction coefficients from Schlafly & Finkbeiner (2011). Although their extinction coefficients are $\sim 20\%$ smaller than our default YREC-based values, the difference has only a moderate effect on the resulting MDFs; the overall shape of the MDFs does not change significantly, because of the small level of foreground dust toward these high Galactic latitude stars.

The photometric MDFs are insensitive to our adopted $[\alpha/\text{Fe}]$ and age scheme (Section 2.1). Even if we had taken a different $[\alpha/\text{Fe}]$ or age relation as a function of $[\text{Fe}/\text{H}]$, model colors would still be forced to match the same set of cluster data from our color calibration procedure (Section 2.2). The resulting

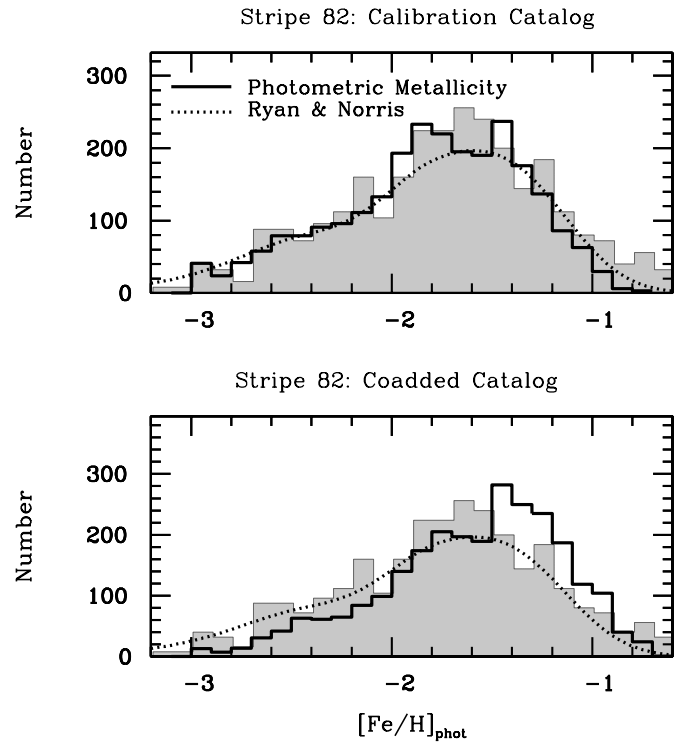


Figure 16. Photometric MDFs of the halo (black solid histograms). The top panel shows the MDF from the calibration catalog and the bottom panel shows the MDF from the co-added catalog. Our MDFs are complete for $[\text{Fe}/\text{H}]_{\text{true}} \leq -1.2$. The overlaid gray shaded histograms are MDFs for the kinematically selected local halo stars from Ryan & Norris (1991b), for which the sample size has been multiplied by a factor of eight, in order to facilitate comparison with the photometric MDFs. The dotted line is the MDF from the same set of stars (Ryan & Norris 1991b), but after convolving it with the photometric convolution kernels (Figure 10), in order to simulate the effects of photometric errors and unresolved binaries and/or blends (see the text).

color- $[\text{Fe}/\text{H}]$ relation would then be essentially unaffected by this change. Although intrinsically broad distributions in $[\alpha/\text{Fe}]$ and/or age at each $[\text{Fe}/\text{H}]$ could result in additional spreading of the observed MDFs, we neglect their effects in the following discussion.

Figure 16 compares our photometric MDFs with the spectroscopic MDF obtained by Ryan & Norris (1991b, gray shaded), which is based on a kinematically selected sample of 372 local halo subdwarfs ($d_{\text{helio}} \lesssim 400$ pc). We have multiplied their sample by a factor of eight to directly compare the shapes of MDFs. The mean $[\text{Fe}/\text{H}]$ value in the Ryan & Norris (1991b) sample is -1.80 over $-3 < [\text{Fe}/\text{H}] < -1$, with a standard deviation of 0.46 dex. Note that, according to these authors, their sample is incomplete above $[\text{Fe}/\text{H}] = -1$.

The abundance measurements in Ryan & Norris (1991b) are accurate to $\sigma \sim 0.2$ dex, while our photometric metallicity estimates have larger dispersions and asymmetric error distributions. In order to perform an “apples-to-apples” comparison with our photometric MDFs, we convolved the MDF of Ryan & Norris (1991b) with the convolution kernels in Figure 10. We binned their data at $[\text{Fe}/\text{H}] < -1$ with intervals of $\Delta[\text{Fe}/\text{H}] = 0.1$ dex, and applied the convolution kernels to each bin, ignoring spectroscopic $[\text{Fe}/\text{H}]$ errors in Ryan & Norris. The resulting MDF is shown (with an arbitrary normalization) as a dotted line in Figure 16, which includes the effects of both photometric errors and unresolved binaries and/or blending, as in our photometric MDFs. The Ryan & Norris (1991b) MDFs are similar

in their overall shape, both before and after the convolution is applied, and both match our in situ MDFs rather well.

As shown in Figure 10, there is a systematic shift in the metallicity scale in the co-added catalog. A Kolmogorov–Smirnov (K-S) test rejects the null hypothesis that the MDF of Ryan & Norris (1991b) and that of the co-added catalog (bottom panel) are drawn from the same parent population at significant levels ($p < 0.001$). On the other hand, the null hypothesis that the Ryan & Norris MDF and that of the calibration catalog (top panel) are drawn from the same parent population cannot be rejected ($p = 0.364$); in other words, their MDFs are statistically similar with each other. Photometric zero-point shifts may be responsible for the systematically higher photometric $[\text{Fe}/\text{H}]$ estimates in the co-added catalog (Section 3.1 and see below in Section 4.2.2).

Perhaps the overall good agreement between our photometric MDFs and the spectroscopic Ryan & Norris (1991b) MDFs should not be so surprising, given the similar range of Galactocentric distances of these two samples. The Ryan & Norris (1991b) stars occupy a local volume (although their orbits extend to much larger distances), at roughly 8 kpc away from the Galactic center. Our sample stars in Stripe 82 are found at present distances within 7–14 kpc from the Galactic center, as shown in Figure 13, although they are much farther away from the Galactic disk than the Ryan & Norris (1991b) sample stars. It is worth keeping in mind that, although we do not presently have full space motions for the stars in our photometric MDFs, they surely contain many stars with orbits that take them far outside the local volume. Both samples of stars can be thought of as local “snapshots” of a volume in the relatively nearby halo.

4.2. Deconvolution of the Halo Metallicity Distribution

We now describe our attempts to recover the “true” halo MDF, using experiments that consider different ways for understanding the nature of the underlying $[\text{Fe}/\text{H}]$ distributions. This requires confronting the possibility that more than one parent stellar population may be required, as discussed below.

We began by deconvolving the observed MDFs of the halo using a single $[\text{Fe}/\text{H}]_{\text{phot}}$ profile (one of the kernels in Figure 10), where a single $[\text{Fe}/\text{H}]_{\text{true}}$ is assumed, without an intrinsic dispersion. We found that none of these profiles are able to match the overall shape of the MDFs, immediately suggesting that either the hypothesis of a small dispersion in $[\text{Fe}/\text{H}]_{\text{true}}$ should be abandoned, and/or at least two sub-components are required to properly account for the overall shape of the MDF. We consider each of these two cases in turn below.

4.2.1. A One-component Model

Figure 17 shows the fitting results for the observed photometric MDFs, assuming that the metallicity of the underlying halo population can be well described by a single Gaussian distribution with a dispersion in metallicity. The solid red line in Figure 17 shows the resulting fit, obtained using the nonlinear least-squares fitting routine MPFIT (Markwardt 2009) over $-2.8 < [\text{Fe}/\text{H}]_{\text{phot}} < -1.0$, after application of the convolution kernels (Figure 10). As described earlier, each of these simulated profiles includes the effects of photometric errors ($\sigma_{g,r,i} = 0.02$ mag, $\sigma_{u,z} = 0.03$ mag) and a 50% unresolved binary fraction and/or blends with the M35 mass function for secondaries. Note that these kernels are not Gaussian functions, nor are they the products of a chemical evolution model.

For the calibration catalog (top panel), we found that a best-fitting Gaussian has a peak at $[\text{Fe}/\text{H}]_{\text{true}} = -1.80 \pm 0.02$ with

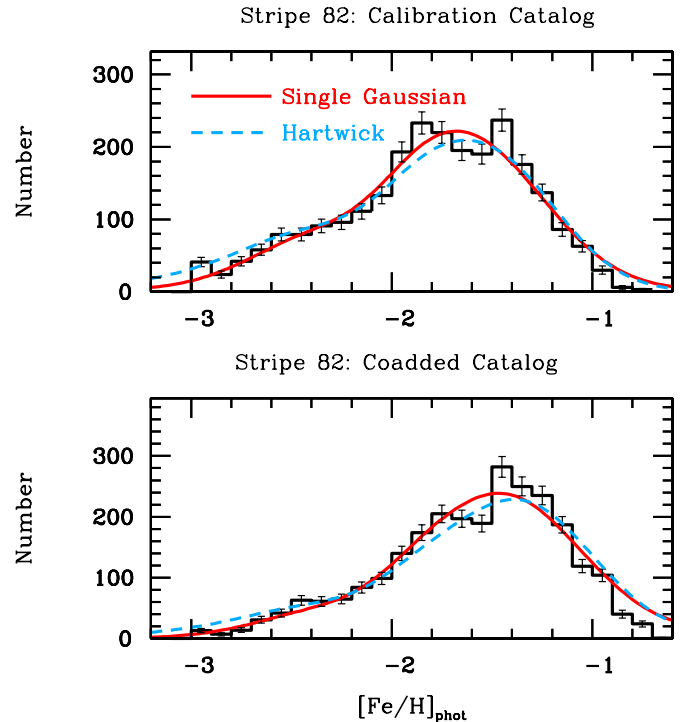


Figure 17. Deconvolution of photometric MDFs of the halo using a single Gaussian $[\text{Fe}/\text{H}]$ distribution. Histograms are observed MDFs from the calibration (top) and the co-added catalog (bottom), respectively. The error bars represent $\pm 1\sigma$ Poisson errors. The solid red line shows an error-convolved $[\text{Fe}/\text{H}]_{\text{phot}}$ distribution from the deconvolution kernels in Figure 10, with a peak of the underlying $[\text{Fe}/\text{H}]$ distribution at $[\text{Fe}/\text{H}] = -1.80$ for the calibration catalog (top), and a peak at $[\text{Fe}/\text{H}] = -1.55$ for the co-added catalog (bottom), respectively, both with dispersions of 0.4 dex. The dashed blue line is the best-fitting simple chemical evolution model from Hartwick (1976), after applying the deconvolution kernels.

(A color version of this figure is available in the online journal.)

$\sigma_{[\text{Fe}/\text{H}]} = 0.41 \pm 0.03$ dex. The reduced χ^2 value (χ^2_{ν}) of the fit is 2.0 for 15 degrees of freedom, assuming Poisson errors. The errors in the above parameters were scaled based on the χ^2_{ν} of the fit. The estimated peak $[\text{Fe}/\text{H}]$ and the dispersion are similar to those obtained for the Ryan & Norris (1991b) sample, as expected from the similar MDF shape from these two studies. For the co-added catalog (bottom panel), we found a best-fitting Gaussian with a peak at $[\text{Fe}/\text{H}]_{\text{true}} = -1.55 \pm 0.03$ and $\sigma_{[\text{Fe}/\text{H}]} = 0.43 \pm 0.04$ dex, with $\chi^2_{\nu} = 2.7$.

For an additional test, we assumed that the photometric MDF is shaped primarily by large photometric errors, even though the underlying $[\text{Fe}/\text{H}]$ distribution is single-peaked at around $[\text{Fe}/\text{H}] = -1.6$. We found marginal agreement with the observed MDFs only if the size of photometric errors were underestimated by a factor of two (i.e., $\sigma_{g,r,i} \approx 0.04$ mag, $\sigma_{u,z} \approx 0.06$ mag) for both of the Stripe 82 catalogs. However, we consider it unlikely that the errors have been underestimated by this much. This hypothesis is also inconsistent with the intrinsically wide range of spectroscopic $[\text{Fe}/\text{H}]$ determinations from Ryan & Norris (1991b).

The dashed blue line in Figure 17 shows the best-fitting simple chemical evolution model (Hartwick 1976). We used the mass-loss modified version as in Ryan & Norris (1991b), who found an excellent match of this model to their MDF. The model MDF is characterized by a single parameter, the effective yield (y_{eff}), which relates to the mass of ejected metals relative to the mass locked in stars. The simple mass-loss modified model

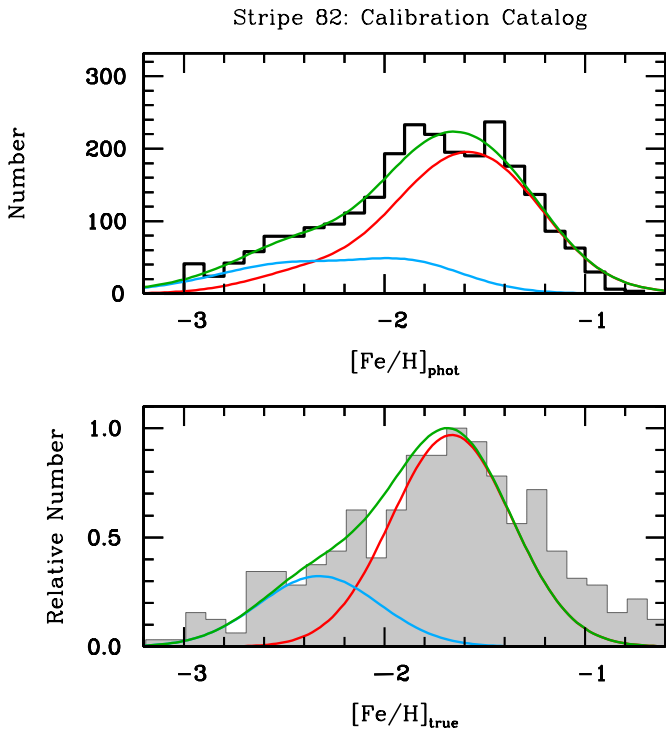


Figure 18. Top: deconvolution of the photometric MDF of the halo from the calibration catalog, using a double Gaussian $[\text{Fe}/\text{H}]$ distribution. Convolution kernels (Figure 10) are applied to the underlying $[\text{Fe}/\text{H}]$ distribution to simulate effects of photometric errors and unresolved binaries and/or blends in the sample. The red and blue curves show a convolved $[\text{Fe}/\text{H}]_{\text{phot}}$ distribution from each component of the double Gaussian distribution. The green curve is the sum of these contributions. The standard deviation of the Gaussians are set to $\sigma_{[\text{Fe}/\text{H}]} = 0.30$ dex. Bottom: the true underlying $[\text{Fe}/\text{H}]$ distribution, as derived from the $[\text{Fe}/\text{H}]_{\text{phot}}$ deconvolution shown in the top panel. The red and blue curves are the underlying $[\text{Fe}/\text{H}]_{\text{true}}$ distributions, with peaks at $[\text{Fe}/\text{H}] = -1.67$ and -2.33 , and the green curve is the sum of these two. The gray histogram shows the observed $[\text{Fe}/\text{H}]$ distribution from Ryan & Norris (1991b), normalized to the peak of the distribution.

(A color version of this figure is available in the online journal.)

adopts instantaneous recycling and mixing of metal products in a leaky box, and further assumes a zero initial metallicity, constant initial mass function, and a fixed effective yield. We utilized $[\text{Fe}/\text{H}]$ in this model as a surrogate for the metallicity. After convolving the model MDF with the deconvolution kernels (Figure 10), we found $\log_{10} y_{\text{eff}} = -1.65 \pm 0.02$ ($\chi^2_{\nu} = 2.6$ for 15 degrees of freedom) for the calibration catalog, and $\log_{10} y_{\text{eff}} = -1.37 \pm 0.04$ ($\chi^2_{\nu} = 5.0$) for the co-added catalog, which simply correspond to the peak of the MDF. The goodness of the fit to the calibration catalog data is comparable to that using the single Gaussian fit, and the resulting effective yield is close to what Ryan & Norris (1991b) obtained from their MDF ($\log_{10} y_{\text{eff}} = -1.6$).

4.2.2. A Two-component Model

Although a single-peak Gaussian $[\text{Fe}/\text{H}]$ distribution describes the observed photometric MDF rather well, it is not a unique solution. Here we consider a two-peak Gaussian $[\text{Fe}/\text{H}]$ distribution fit to the Stripe 82 MDFs.

The red and blue curves in the top panel of Figure 18 show the best-matching pair of simulated profiles to the calibration catalog MDF, searched using the MPFIT routine over $-2.8 < [\text{Fe}/\text{H}]_{\text{phot}} < -1.0$. In this fitting exercise, we fixed the dispersion of the underlying $[\text{Fe}/\text{H}]$ distributions to $\sigma_{[\text{Fe}/\text{H}]} = 0.30$ dex for both Gaussians. The green curve is the sum of

these individual components, which exhibits an excellent fit to the observed profile ($\chi^2_{\nu} = 1.9$ for 14 degrees of freedom). The underlying true $[\text{Fe}/\text{H}]$ distribution for each of these curves is shown in the bottom panel, which exhibits peaks at $[\text{Fe}/\text{H}]_{\text{true}} = -1.67 \pm 0.08$ and -2.33 ± 0.30 , respectively.

The bottom panel in Figure 18 also shows the spectroscopic MDF from Ryan & Norris (1991b, gray histogram). Our deconvolved $[\text{Fe}/\text{H}]$ distribution matches their observed MDF well on the metal-poor side. Their sample is contaminated by disk stars above $[\text{Fe}/\text{H}] \approx -1$, while our photometry sample selection excludes metal-rich stars with $[\text{Fe}/\text{H}]_{\text{true}} > -1.2$ (Section 3.1).

The fractional contribution of the low-metallicity component with a peak at $[\text{Fe}/\text{H}]_{\text{true}} = -2.33$ (the area under the blue curve in the top panel of Figure 18) to the entire halo sample (the area under the green curve in the top panel) is 24%, with a clear strong dependence on metallicity. Below $[\text{Fe}/\text{H}] = -2.0$, the contribution from the low-metallicity component is 52% of the total numbers of halo stars in this metallicity regime. Above $[\text{Fe}/\text{H}] = -1.5$, the high-metallicity component (the red curve with a peak at $[\text{Fe}/\text{H}]_{\text{true}} = -1.67$) contributes 96% of the total numbers of halo stars.

The relative fraction of the low-metallicity component depends on our adopted value for the dispersion of the underlying $[\text{Fe}/\text{H}]$ distribution. In the above exercise, we assumed $\sigma_{[\text{Fe}/\text{H}]} = 0.30$ dex for each component. However, the contribution from the low $[\text{Fe}/\text{H}]$ component becomes as high as 42% if the standard deviation is set to $\sigma_{[\text{Fe}/\text{H}]} = 0.20$ dex. On the other hand, fixing the value to $\sigma_{[\text{Fe}/\text{H}]} = 0.4$ dex leads to a similar result as in the previous section, which requires only one component in the fit. If $\sigma_{[\text{Fe}/\text{H}]} = 0.2$ dex is a reasonable lower limit to the dispersion of each of the underlying $[\text{Fe}/\text{H}]$ components, we can only set an upper limit on the fractional contribution of the low-metallicity component, at $\sim 40\%$ – 50% .

To investigate this further, we have also performed two-component deconvolutions leaving each component's dispersion as a free parameter. For this, we use the *extreme deconvolution* (Bovy et al. 2011) technique, which fits all parameters of arbitrary numbers of Gaussian components to data with individual uncertainties, and which has been extended to handle non-Gaussian uncertainty kernels, such as those in Section 2.5. The best two-component fit (with $\Delta\chi^2 = 6.5$ compared to the fixed $\sigma_{[\text{Fe}/\text{H}]} = 0.3$ dex fit above) consists of a 69% contribution from a low-metallicity component ($[\text{Fe}/\text{H}] = -2$) with $\sigma_{[\text{Fe}/\text{H}]} = 0.35$ dex and a higher-metallicity component ($[\text{Fe}/\text{H}] = -1.4$). However, the latter has an unrealistically small dispersion of only $\sigma_{[\text{Fe}/\text{H}]} = 0.07$ dex. Fitting instead with a weak prior on the dispersion (a χ^2 distribution with 2 degrees of freedom and a mean of 0.3 dex) yields a slightly worse fit ($\Delta\chi^2 = 2$ with respect to the best fit), with almost equal contributions from a low-metallicity (53%, mean $[\text{Fe}/\text{H}] = -2.14$, $\sigma_{[\text{Fe}/\text{H}]} = 0.3$ dex) and a higher-metallicity (mean $[\text{Fe}/\text{H}] = -1.5$, $\sigma_{[\text{Fe}/\text{H}]} = 0.2$ dex) component. These results further show that the parameters of a two-component fit are only poorly constrained on the basis of the photometric-metallicity data alone.

An even stronger constraint on the fraction of the low-metallicity halo component can be obtained if our *deconvolved* MDF is forced to match the shape of the Ryan & Norris (1991b) MDF. As shown in the bottom panel of Figure 18, our assumed $[\text{Fe}/\text{H}]$ dispersion of 0.3 dex results in a good agreement of our MDF with that of the Ryan & Norris sample (gray shaded). However, the agreement breaks down

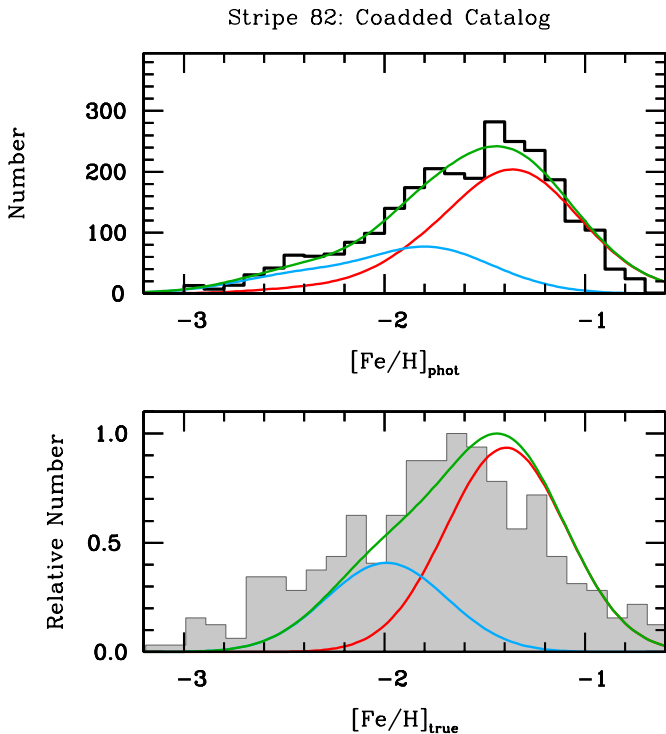


Figure 19. Same as in Figure 18, but for the co-added catalog. The red and blue curves in the bottom panel show the underlying $[\text{Fe}/\text{H}]_{\text{true}}$ distributions with peaks at $[\text{Fe}/\text{H}] = -1.39$ and -1.99 , respectively.

(A color version of this figure is available in the online journal.)

when a smaller (or larger) value is assumed for a dispersion of the individual underlying $[\text{Fe}/\text{H}]$ distributions; a smaller dispersion leads to an enhanced contribution from the metal-poor component, resulting in an overestimated number of metal-poor stars with respect to the Ryan & Norris MDF. From the above considerations, we find that individual components of the underlying MDF with ~ 0.25 – 0.32 dex dispersion in $[\text{Fe}/\text{H}]$ provide a reasonably good fit to the Ryan & Norris (1991b) MDF; in other words, the Ryan & Norris MDF is also well fit by double Gaussians with these dispersion values. The fractions of the low-metallicity component of the halo corresponding to these values are $\sim 20\%$ – 35% of the entire halo population.

In the case of the co-added catalog (Figure 19), the overall metallicities are shifted toward higher $[\text{Fe}/\text{H}]$ values; peak $[\text{Fe}/\text{H}]_{\text{true}}$ values of the two components are $[\text{Fe}/\text{H}] = -1.39 \pm 0.12$ and -1.99 ± 0.23 , respectively, with a total χ^2_{ν} value of 2.6. The shift in $[\text{Fe}/\text{H}]$ is expected from the photometric zero-point difference between the two Stripe 82 catalogs (Section 3.1), where the larger (fainter) u -band magnitudes in the co-added catalog produce higher photometric metallicities than in the calibration catalog. The contribution of the metal-poor component is comparable (30%) to that derived from the calibration catalog (24%).

A strong disagreement with the Ryan & Norris (1991b) MDF is evident in the lower panel, where the deconvolved MDF shows systematically higher metallicities. If we expect both MDFs to be the same at similar Galactocentric distances, this would indicate that the MDF in Figure 19 has been shifted toward higher $[\text{Fe}/\text{H}]$ due to photometric zero-point errors in the co-added catalog (Section 3.1). Some of the stars in Stripe 82 have spectroscopic estimates from the SSPP and were included in the comparison of the spectroscopic metallicities with the

photometric determinations (Section 2.4). However, there were not a sufficient number of stars satisfying both the spectroscopic (Section 2.4) and photometric (Section 3.1) selection criteria for a meaningful comparison to verify which photometric catalog provides a more consistent result with the SSPP estimates.

Our results illustrate a simple limiting case, where one could imagine that the stellar halo formed out of individual subhalos which, in the mean, were pre-enriched in metals that peak roughly at the observed locations. Nevertheless, the fact that the observed photometric $[\text{Fe}/\text{H}]$ distribution is well described by primarily two metallicity peaks at $[\text{Fe}/\text{H}] \sim -1.7$ and -2.3 is consistent with the argument by Carollo et al. (2007, 2010) that our Milky Way stellar halo is a superposition of at least two components, the inner and outer halos, that are distinct in metallicity, kinematics, and spatial distributions. The apparent duality of the Galactic halo system is further supported by a limited kinematic analysis of stars in our photometric sample, as described below (Section 4.3). It should be kept in mind that our description of these two populations, following Carollo et al., assumes that they are “smooth” distributions, even though it is recognized that there exist numerous, possibly even locally dominant, examples of substructure (such as stellar streams and overdensities) being present as well.

From the above tests, we conclude that we do not have sufficiently strong constraints, from the observed photometric MDFs alone, in order to discriminate between the hypothesis of the duality of the halo (Figures 18 and 19) and the single stellar population (Figure 17) model. We also cannot preclude the possibility that the halo comprises more than two sub-components, because of the limited number of constraints presented by the observed MDFs to perform multi-component fitting. However, we show below that the degeneracy in this solution can be at least partially removed by combining independent information from the available kinematics of our sample stars, as well as for those in the Ryan & Norris (1991b) sample.

4.3. Metallicity Correlations with Kinematics

Most of the stars in our Stripe 82 photometric sample do not have full velocity information available. However, at high Galactic latitudes, proper-motion measurements alone can provide useful constraints on the U (toward the Galactic center) and V (in the direction of Galactic disk rotation) velocity components, which are sufficient to constrain the motions of stars parallel to the Galactic plane.

We searched for proper-motion measurements in SDSS (Munn et al. 2004), with the proper-motion flags set to the recommended values: `match = 1`, `nFit = 6` and `dist22 > 7`, `sigRa < 525`, and `sigDec < 525` (taking into account the correction described by Munn et al. 2008). We then combined proper-motion measurements with our distance estimates to compute *approximate* rotation velocities¹⁶ (v_{ϕ}) in the Galactocentric cylindrical system (see Bond et al. 2010).

Figure 20 shows the approximate velocity distribution in v_{ϕ} for the calibration and co-added catalogs, respectively. The top panels show the full velocity distribution of all stars in each catalog, while the middle and bottom panels show subsets of these in the metal-rich ($-1.5 < [\text{Fe}/\text{H}] \leq -1.0$; middle panel) and in the metal-poor ($-3.0 < [\text{Fe}/\text{H}] \leq -2.0$; bottom panel) regimes, respectively. Inspection of the distributions in these two metallicity ranges indicates that they are not identical, as

¹⁶ Below we use V_{ϕ} to represent a rotational velocity computed using the full kinematic information, to distinguish it from v_{ϕ} .

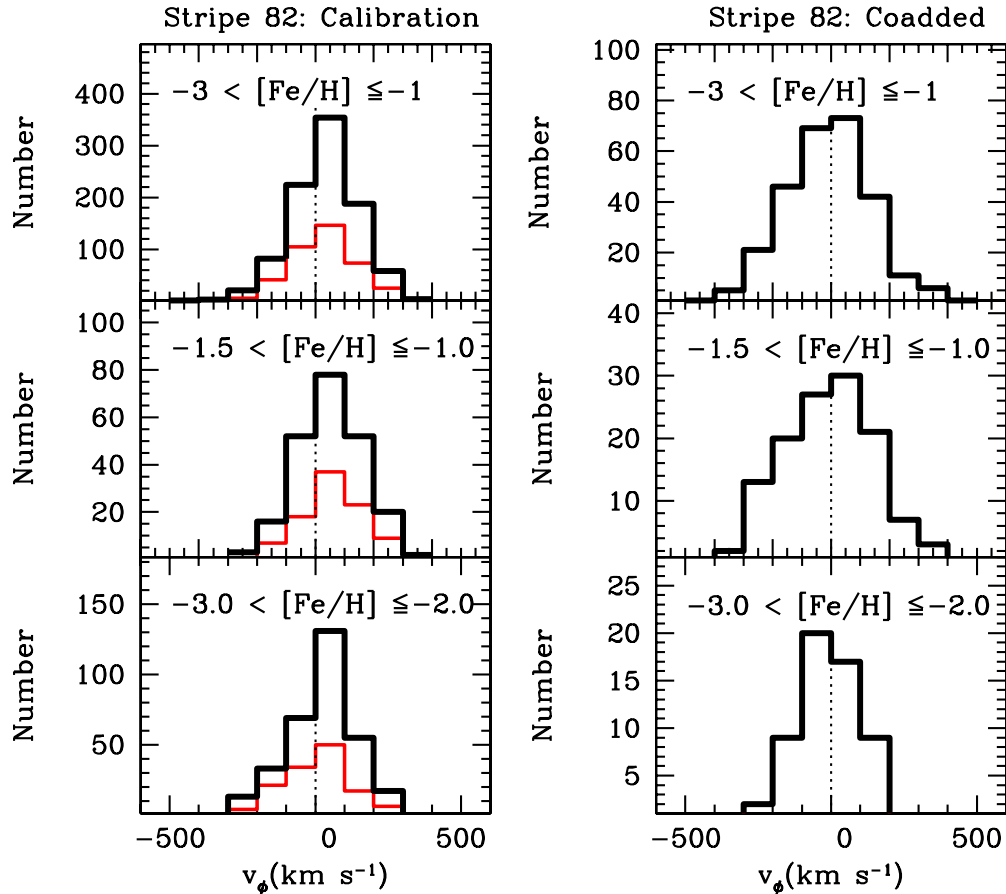


Figure 20. Distribution of approximate rotation velocity in the Galactocentric cylindrical system (v_ϕ) for the calibration (left panels) and the co-added (right panels) catalogs. The thick black and thin red histograms are those based on stars at $|b| > 45^\circ$ and $|b| > 60^\circ$, respectively. The top to bottom panels show the sample in different metallicity bins. A vertical dotted line is shown at zero rotation.

(A color version of this figure is available in the online journal.)

might be expected for a single halo population. The thick black histograms show the v_ϕ distributions of stars at $|b| > 45^\circ$; red histograms show the more restricted case with $|b| > 60^\circ$ (the restriction to higher latitude provides a better approximation for the rotational velocity). Comparisons between the black and red histograms show that the latitudinal restrictions only mildly change the overall distributions in all metallicity bins. For the calibration catalog, a K-S test rejects the null hypothesis that the samples in the two different metallicity ranges are drawn from the same parent population at significant levels ($p = 0.019$ for $|b| > 45^\circ$; $p = 0.003$ for $|b| > 60^\circ$). For the co-added catalog, the K-S test is unable to reject this hypothesis ($p = 0.167$ for $|b| > 45^\circ$; $p = 0.297$ for $|b| > 60^\circ$). Although not a strong effect, there exist greater fractions of more metal-poor halo stars in retrograde, rather than prograde, rotation for both catalogs.

A more striking difference is obtained when the MDFs are considered for different v_ϕ ranges, as shown in Figure 21. As before, the black and red histograms indicate the two samples at different Galactic latitude ranges. The middle panels show the MDFs for stars with high prograde rotation ($v_\phi > 80 \text{ km s}^{-1}$); bottom panels show those of stars with extreme retrograde rotation ($v_\phi < -80 \text{ km s}^{-1}$). Note that the $\pm 80 \text{ km s}^{-1}$ limit was set in order to maximize the numbers of stars in each split, so as to enable statistically meaningful interpretations.

Inspection of Figure 21 indicates that the MDFs for stars in retrograde motion are shifted toward lower metallicities than

the MDFs for those in prograde rotation. For the calibration catalog, whether the samples are restricted to $|b| > 45^\circ$ or $|b| > 60^\circ$, a K-S test rejects the null hypothesis that the two samples for different ranges of v_ϕ are drawn from the same parent population at highly significant levels ($p = 0.0001$ for $|b| > 45^\circ$; $p = 0.0002$ for $|b| > 60^\circ$). For the co-added catalog, the lower-latitude cut results in a significant rejection ($p = 0.026$ for $|b| > 45^\circ$); no rejection can be made for $|b| > 60^\circ$ ($p = 0.257$). We conclude that greater fractions of low-metallicity halo stars exist in retrograde, rather than prograde, rotation.

Inspired by these results, we decided to check how the MDFs of the spectroscopic Ryan & Norris (1991b) sample vary for prograde versus retrograde rotation, and how the V_ϕ distributions vary for higher- and lower-metallicity divisions. Note that we distinguish V_ϕ from v_ϕ to indicate the fact that the rotation component for the Ryan & Norris sample is obtained from full space motions (Ryan & Norris 1991a). Figure 22 shows the $[\text{Fe}/\text{H}]$ distributions (left panels) and V_ϕ distributions (right panels) of their locally kinematically selected sample, with the same limits as on v_ϕ and $[\text{Fe}/\text{H}]$ in Figures 20 and 21, except in the middle left panel, where we set $V_\phi > 50 \text{ km s}^{-1}$ to include a sufficient number of stars. Clear differences exist in these distributions. A K-S test indicates that the null hypothesis that the samples are drawn from the same parent population is rejected at significant levels: $p = 0.019$ for the different ranges in V_ϕ and $p = 0.021$ for the different ranges in $[\text{Fe}/\text{H}]$.

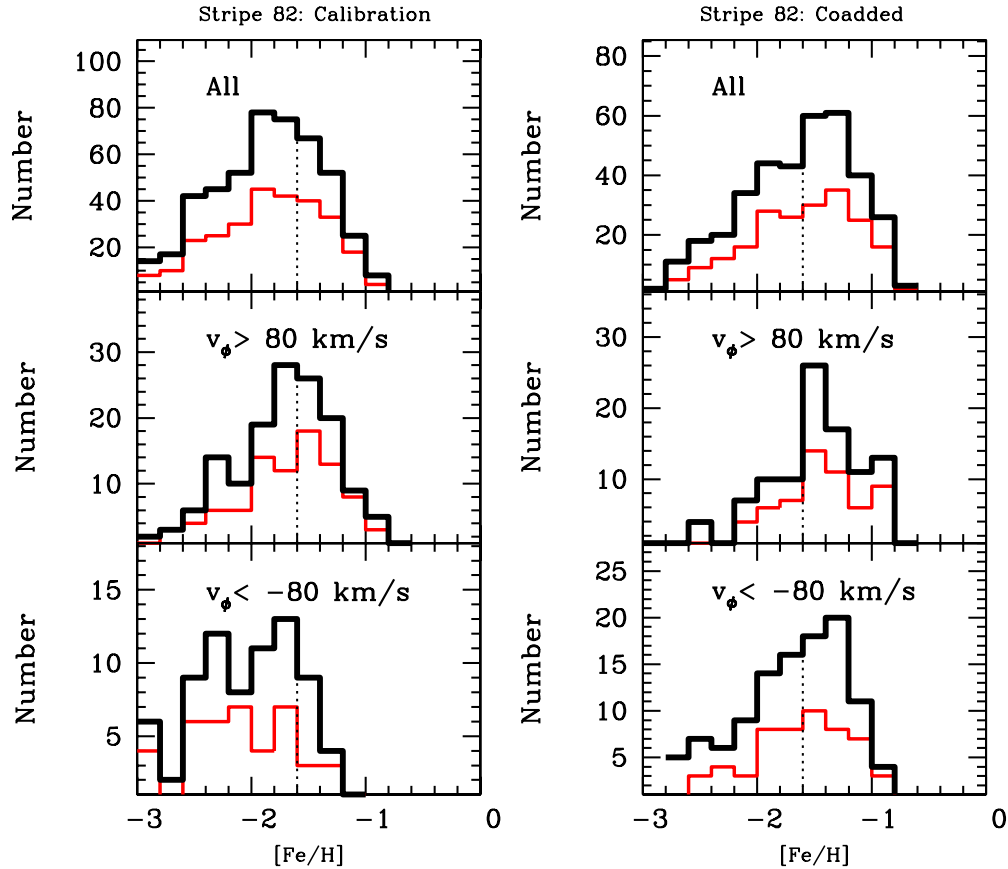


Figure 21. MDFs in different bins of approximate rotational velocity in the Galactocentric cylindrical system (v_ϕ) for the calibration (left panels) and the co-added (right panels) catalogs. The thick black and thin red histograms are those based on stars at $|b| > 45^\circ$ and $|b| > 60^\circ$, respectively. A vertical dotted line at $[\text{Fe}/\text{H}] = -1.5$ is shown for reference.

(A color version of this figure is available in the online journal.)

Both divisions indicate that greater fractions of metal-poor halo stars are found in retrograde, rather than prograde, rotation.

Table 3 summarizes the average $[\text{Fe}/\text{H}]$ values (and errors in the mean) for the kinematically divided samples considered above. For the calibration and coadded catalogs, the mean $[\text{Fe}/\text{H}]$ is between -1.7 and -1.5 for stars in highly prograde motion ($v_\phi > 80 \text{ km s}^{-1}$). For the calibration catalog, the mean $[\text{Fe}/\text{H}]$ for the highly retrograde components ($v_\phi < -80 \text{ km s}^{-1}$) is ~ 0.3 – 0.4 dex lower than for the metal-rich counterparts; the difference is ~ 0.2 dex for the co-added catalog. The difference in the mean $[\text{Fe}/\text{H}]$ between the highly retrograde component and the highly prograde component in the Ryan & Norris (1991b) sample is 0.3 dex. Taken as a whole, these simple kinematic divisions indicate that a single stellar population is inadequate to describe the behavior of the higher and lower-metallicity halo stars for all three samples.

We caution that the observed kinematic–metallicity correlation can also be produced by (sub)giant contamination in our sample (e.g., Ryan 1989). Unrecognized giants and subgiants are brighter than dwarfs, so their distances and velocities will be underestimated, while their photometric metallicities are higher than those for dwarfs (Figure 14). We used the photometry of M13 (An et al. 2008) to perform the same suite of simple Galactic halo models as in Section 3.2, and found that (sub)giants have systematically higher photometric metallicities, and higher v_ϕ , than dwarfs. The overall contamination rate of (sub)giants in the sample is estimated around 15%, but the fraction increases to $\sim 40\%$ when high-metallicity

stars ($-1.5 < [\text{Fe}/\text{H}] < -1.0$) are considered. However, it is less likely that the observed kinematic–metallicity correlation is caused entirely by the (sub)giant contamination, because the Ryan & Norris sample, which is independent from our photometric sample and has different selection criteria, also exhibits the same behavior (Figure 22). Further investigation is needed on the effect of (sub)giant contamination.

5. SUMMARY AND DISCUSSION

We have used a new, empirically calibrated set of stellar isochrones to derive distances, temperatures, and metallicities for individual stars in SDSS Stripe 82 using *ugriz* photometry. These estimates have been validated by comparisons with the IRFM temperature scale and SDSS/SEGUE medium-resolution spectroscopic values. Based on unbiased photometric samples of main-sequence Stripe 82 stars in a relatively narrow mass range, we have constructed an in situ MDF of the Galactic halo in the distance range 5–8 kpc from the Sun, which is similar in shape to that of the local kinematically selected subdwarfs in Ryan & Norris (1991b). This MDF can be adequately fit using a single Gaussian with peak at $[\text{Fe}/\text{H}] = -1.5$ and a broad (0.4 dex) dispersion of metallicities. However, an equally valid fit can be obtained from the use of two components with peaks at $[\text{Fe}/\text{H}] \approx -1.7$ and -2.3 , with smaller dispersions (0.25–0.32 dex). For an adopted dispersion of 0.3 dex, on the order of 25% of the stars in our local halo sample can be associated with the low-metallicity component.

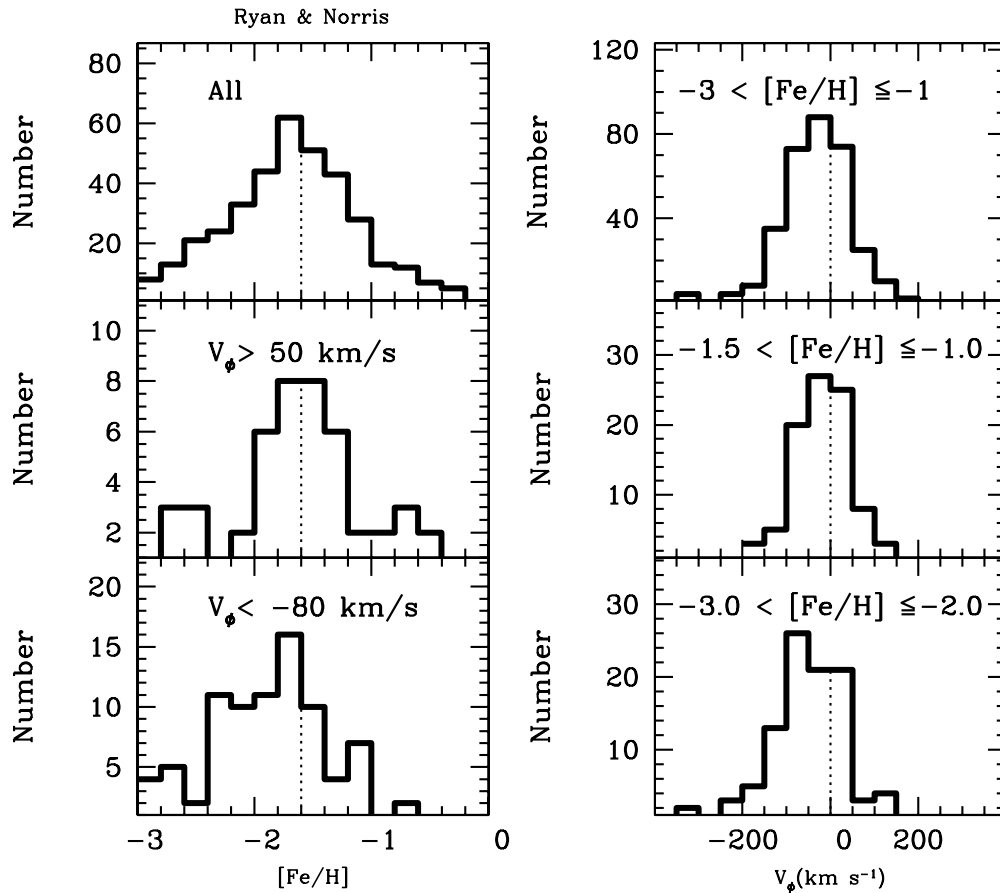


Figure 22. Same as in Figures 20 and 21, but for the local kinematically selected sample of Ryan & Norris (1991b). Note that we distinguish V_ϕ from v_ϕ to indicate the fact that the rotation component for the Ryan & Norris sample is obtained from full space motions. The vertical dotted line is shown in the left panels for $[\text{Fe}/\text{H}] = -1.6$, and at zero rotation in the right panels, for reference.

Table 3
Mean $[\text{Fe}/\text{H}]$ of Kinematically Separated Samples

Sample	Latitudinal restriction	$v_\phi > 80 \text{ km s}^{-1}$		$v_\phi < -80 \text{ km s}^{-1}$	
		$\langle [\text{Fe}/\text{H}] \rangle$	N	$\langle [\text{Fe}/\text{H}] \rangle$	N
Stripe 82 calibration	$ b > 60^\circ$	-1.69 ± 0.05	89	-2.08 ± 0.08	41
Stripe 82 calibration	$ b > 45^\circ$	-1.72 ± 0.04	143	-2.05 ± 0.05	75
Stripe 82 co-added	$ b > 60^\circ$	-1.47 ± 0.05	59	-1.63 ± 0.06	56
Stripe 82 co-added	$ b > 45^\circ$	-1.51 ± 0.04	102	-1.69 ± 0.05	111
Ryan & Norris (1991b) ^a	...	-1.59 ± 0.09^b	47	-1.90 ± 0.07	88

Notes.

^a Rotation component for the Ryan & Norris sample obtained from full space motions (V_ϕ) is used to divide the sample in the above table.

^b $V_\phi > 50 \text{ km s}^{-1}$ was used.

For stars with $[\text{Fe}/\text{H}] < -2.0$, this fraction increases to on the order of 50%. For stars with $[\text{Fe}/\text{H}] > -1.5$, essentially all of the stars are associated with the high-metallicity component. If a smaller dispersion is adopted (0.2 dex), $\sim 40\%$ – 50% of the total halo sample can be associated with the low-metallicity component, but would make the deconvolved photometric MDF different in shape from that of the local Ryan & Norris (1991b) kinematically selected sample. Our analysis cannot preclude the possibility that more than two sub-components could exist in the halo.

A limited kinematic analysis of the stars in our photometric sample, based on approximation of the rotational motions of stars about the Galactic center (derived from available proper motions at high Galactic latitude), indicates that the metal-

poor and metal-rich subsamples exhibit different behaviors, suggesting that the dual-component model is likely to be superior to the single-component model. Greater fractions of metal-poor stars ($[\text{Fe}/\text{H}] < -2.0$) in the halo possess retrograde orbits, as compared to more metal-rich stars ($-1.5 < [\text{Fe}/\text{H}] < -1.0$), consistent with the claim by Carollo et al. (2007, 2010) that the halo comprises two overlapping systems, an inner-halo population and an outer-halo population, with similar metallicity–kinematic correlations as we find from our present analysis. The observed behaviors of these halo stars are also consistent with theoretical expectations from Milky-Way-like galaxies, where inner-spheroid stars primarily formed in the main progenitor(s) of the galaxy and exhibit net prograde rotation, while the accreted outer-halo component exhibits a

mild degree of rotation, or in a minority of cases, a retrograde rotation (McCarthy et al. 2012).

We have also considered an independent sample of halo stars, one that is still in common use for describing the MDF of the Milky Way's halo. Ryan & Norris (1991b) found that their derived halo MDF (based on a local kinematically selected sample) can be well described by a simple chemical evolution model (Hartwick 1976). Our local in situ halo MDF is also well fit by this model. However, there are a number of unphysical assumptions that are made by such a model, including instantaneous recycling and mixing of metals throughout the entire halo, as well as the use of a so-called effective yield (by which the metals produced by individual supernovae are reduced by an arbitrary amount, one that is not predicted by present understanding, but acts only as a fitting parameter of the model). Such limitations immediately call into question the applicability of these classes of models in the context of a presumed hierarchical assembly of the Galactic halo from individual lower-mass subhalos. Such a model (at least when applied to the halo as a whole) clearly presumes that the stars belong to a single population. As was the case for our analysis of the unbiased photometric stellar halo sample, our investigation of the rotational behavior of the Ryan & Norris data also does not support a single-population model.

Our current understanding on the nature of the halo provides caveats for the use and interpretation of the observed MDFs. For example, Schörck et al. (2009) and Li et al. (2010) consider halo MDFs based on spectroscopic follow-up of candidate metal-poor stars from the Hamburg/ESO survey. Below $[\text{Fe}/\text{H}] = -2.5$, the MDFs of both samples (the first comprising mainly giants, the second comprising mostly dwarfs) appear in excellent agreement with one another, and led to the conclusion that there existed a sharp low-metallicity cutoff (at $[\text{Fe}/\text{H}] = -3.6$), below which fewer than expected numbers of the lowest metallicity stars were found. For stars with higher metallicity, these authors argue that the observed MDFs of the two samples differ from one another due to the very different selection biases on metallicity involved for the cooler (giants) and warmer (dwarfs) samples. However, if the halo comprises two overlapping stellar components (Carollo et al. 2007, 2010; Beers et al. 2012), the different behaviors of the giant and dwarf samples are likely to be strongly influenced by the degree to which the inner- and outer-halo populations contribute to them, convolved with the clearly present selection biases, rather than being due to the selection bias alone. The implication of the dual nature of the halo is that the subject under discussion is *not* the tail of the MDF of “the halo,” but rather, the tail of the MDF of the outer-halo population, with clear implications for the origin of this component. Further investigations of these connections would be of great interest.

D.A. thanks Gerry Gilmore for helpful comments. We also thank Brian Yanny and James Annis for useful discussions. D.A. acknowledges support by the Ewha Womans University Research Grant of 2010. Support for this work was provided by the National Research Foundation of Korea to the Center for Galaxy Evolution Research (No. 2010-0027910). T.C.B. and Y.S.L. acknowledge partial support of this work from grants PHY 02-16783 and PHY 08-22648: Physics Frontiers Center/Joint Institute for Nuclear Astrophysics (JINA), awarded by the U.S. National Science Foundation. J.A.J. acknowledges support from NSF grant AST-0707948. M.P. acknowledges support from NASA Astrophysics Theory Program grant NNX11AE04G. Ž.I. acknowledges support by NSF

AST-1008784 to the University of Washington and by NSF grant AST-0551161 to LSST for design and development activity. J.B. acknowledges support provided by NASA through Hubble Fellowship grant HST-HF-51285.01 awarded by the Space Telescope Science Institute, which is operated by the Association of Universities for Research in Astronomy, Incorporated, under NASA contract NAS5-26555. M.N. acknowledges support from NSF grant AST-1009670.

Funding for SDSS and SDSS-II has been provided by the Alfred P. Sloan Foundation, the Participating Institutions, the National Science Foundation, the U.S. Department of Energy, the National Aeronautics and Space Administration, the Japanese Monbukagakusho, the Max Planck Society, and the Higher Education Funding Council for England. The SDSS Web site is <http://www.sdss.org/>.

The SDSS is managed by the Astrophysical Research Consortium for the Participating Institutions. The Participating Institutions are the American Museum of Natural History, Astrophysical Institute Potsdam, University of Basel, University of Cambridge, Case Western Reserve University, University of Chicago, Drexel University, Fermilab, the Institute for Advanced Study, the Japan Participation Group, Johns Hopkins University, the Joint Institute for Nuclear Astrophysics, the Kavli Institute for Particle Astrophysics and Cosmology, the Korean Scientist Group, the Chinese Academy of Sciences (LAMOST), Los Alamos National Laboratory, the Max-Planck-Institute for Astronomy (MPIA), the Max-Planck-Institute for Astrophysics (MPA), New Mexico State University, Ohio State University, University of Pittsburgh, University of Portsmouth, Princeton University, the United States Naval Observatory, and the University of Washington.

REFERENCES

- Abazajian, K. N., Adelman-McCarthy, J. K., Agüeros, M. A., et al. 2003, *AJ*, **126**, 2081
- Abazajian, K. N., Adelman-McCarthy, J. K., Agüeros, M. A., et al. 2004, *AJ*, **128**, 502
- Abazajian, K. N., Adelman-McCarthy, J. K., Agüeros, M. A., et al. 2005, *AJ*, **129**, 1755
- Abazajian, K. N., Adelman-McCarthy, J. K., Agüeros, M. A., et al. 2009, *ApJS*, **182**, 543
- Adelman-McCarthy, J. K., Agüeros, M. A., Allam, S. S., et al. 2006, *ApJS*, **162**, 38
- Adelman-McCarthy, J. K., Agüeros, M. A., Allam, S. S., et al. 2007, *ApJS*, **172**, 634
- Adelman-McCarthy, J. K., Agüeros, M. A., Allam, S. S., et al. 2008, *ApJS*, **175**, 297
- Aihara, H., Allende Prieto, C., An, D., et al. 2011, *ApJS*, **193**, 29
- Allende Prieto, C., Sivarani, T., Beers, T. C., et al. 2008, *AJ*, **136**, 2070
- An, D., Johnson, J. A., Beers, T. C., et al. 2009a, *ApJL*, **707**, 64
- An, D., Johnson, J. A., Clem, J. L., et al. 2008, *ApJS*, **179**, 326
- An, D., Pinsonneault, M. H., Masseron, T., et al. 2009b, *ApJ*, **700**, 523
- An, D., Terndrup, D. M., & Pinsonneault, M. H. 2007a, *ApJ*, **671**, 1640
- An, D., Terndrup, D. M., Pinsonneault, M. H., et al. 2007b, *ApJ*, **655**, 233
- Annis, J., Soares-Santos, M., Strauss, M. A., et al. 2011, *ApJ*, submitted (arXiv:1111.6619)
- Barrado y Navascués, D., Stauffer, J. R., Bouvier, J., & Martín, E. L. 2001, *ApJ*, **546**, 1006
- Beers, T. C., Carollo, D., Ivezić, Ž., et al. 2012, *ApJ*, **746**, 34
- Beers, T. C., Preston, G. W., & Shectman, S. A. 1985, *AJ*, **90**, 2089
- Beers, T. C., Preston, G. W., & Shectman, S. A. 1992, *AJ*, **103**, 1987
- Belokurov, V., Zucker, D. B., Evans, N. W., et al. 2006a, *ApJL*, **642**, 137
- Belokurov, V., Zucker, D. B., Evans, N. W., et al. 2006b, *ApJL*, **647**, 111
- Bond, N. A., Ivezić, Ž., Sesar, B., et al. 2010, *ApJ*, **716**, 1
- Bovy, J., Hogg, D. W., & Roweis, S. T. 2011, *AnApS*, **5**, 1657
- Bovy, J., Myers, A. D., Hennawi, J. F., et al. 2012a, *ApJ*, **749**, 41
- Bovy, J., Rix, H.-W., & Hogg, D. W. 2012b, *ApJ*, **751**, 131
- Bullock, J. S., & Johnston, K. V. 2005, *ApJ*, **635**, 931

- Brown, T. M., Latham, D. W., Everett, M. E., & Esquerdo, G. A. 2011, *AJ*, **142**, 112
- Cardelli, J. A., Clayton, G. C., & Mathis, J. S. 1989, *ApJ*, **345**, 245
- Carney, B. W. 1979, *ApJ*, **233**, 211
- Carney, B. W., Laird, J. B., Latham, D. W., & Aguilar, L. A. 1996, *AJ*, **112**, 668
- Carollo, D., Beers, T. C., Bovy, J., et al. 2012, *ApJ*, **744**, 195
- Carollo, D., Beers, T. C., Chiba, M., et al. 2010, *ApJ*, **712**, 692
- Carollo, D., Beers, T. C., Lee, Y. S., et al. 2007, *Natur*, **450**, 1020
- Carretta, E., Gratton, R. G., Clementini, G., & Fusi Pecci, F. 2000, *ApJ*, **533**, 215
- Casagrande, L., Ramírez, I., Meléndez, J., Bessell, M., & Asplund, M. 2010, *A&A*, **512**, A54
- Chiba, M., & Beers, T. C. 2000, *AJ*, **119**, 2843
- Christlieb, N. 2003, *RvMA*, **16**, 191
- Christlieb, N., Schörck, T., Frebel, A., et al. 2008, *A&A*, **484**, 721
- Eggen, O. J., Lynden-Bell, D., & Sandage, A. R. 1962, *ApJ*, **136**, 748
- Font, A. S., McCarthy, I. G., Crain, R. A., et al. 2011, *MNRAS*, **416**, 2802
- Girardi, L., Grebel, E. K., Odenkirchen, M., & Chiosi, C. 2004, *A&A*, **422**, 205
- Gunn, J. E., Siegmund, W. A., Mannery, E. J., et al. 2006, *AJ*, **131**, 2332
- Hartwick, F. D. A. 1976, *ApJ*, **209**, 418
- Ivezić, Ž., Sesar, B., Jurić, M., et al. 2008, *ApJ*, **684**, 287
- Ivezić, Ž., Smith, J. A., Miknaitis, G., et al. 2007, *AJ*, **134**, 973
- Johnston, K. V., Bullock, J. S., Sharma, S., et al. 2008, *ApJ*, **689**, 936
- Jurić, M., Ivezić, Ž., Brooks, A., et al. 2008, *ApJ*, **673**, 864
- Kirby, E. N., Guhathakurta, P., & Sneden, C. 2008, *ApJ*, **682**, 1217
- Kraft, R. P., & Ivans, I. I. 2003, *PASP*, **115**, 143
- Lee, Y. S., Beers, T. C., Sivarani, T., et al. 2008a, *AJ*, **136**, 2022
- Lee, Y. S., Beers, T. C., Sivarani, T., et al. 2008b, *AJ*, **136**, 2050
- Li, H. N., Christlieb, N., Schörck, T., et al. 2010, *A&A*, **521**, A10
- Lupton, R. H., Ivezić, Z., Gunn, J. E., et al. 2002, *Proc. SPIE*, **4836**, 350
- Markwardt, C. B. 2009, in ASP Conf. Ser. 411, *Astronomical Data Analysis Software and Systems*, ed. D. A. Bohlender, D. Durand, & P. Dowler (San Francisco, CA: ASP), 251
- McCarthy, I. G., Font, A. S., Crain, R. A., et al. 2012, *MNRAS*, **420**, 2245
- Munn, J. A., Monet, D. G., Levine, S. E., et al. 2004, *AJ*, **127**, 3034
- Munn, J. A., Monet, D. G., Levine, S. E., et al. 2008, *AJ*, **136**, 895
- Nissen, P. E., & Schuster, W. J. 2010, *A&A*, **511**, L10
- Padmanabhan, N., Schlegel, D. J., Finkbeiner, D. P., et al. 2008, *ApJ*, **674**, 1217
- Peng, X., Du, C., & Wu, Z. 2012, *MNRAS*, **422**, 2756
- Pinsonneault, M. H., An, D., Molenda-Žakowicz, J., et al. 2012, *ApJS*, **199**, 30
- Pinsonneault, M. H., Terndrup, D. M., Hanson, R. B., & Stauffer, J. R. 2004, *ApJ*, **600**, 946
- Qian, Y.-Z., & Wasserburg, G. J. 2012, *PNAS*, **109**, 4750
- Ryan, S. G. 1989, *AJ*, **98**, 1693
- Ryan, S. G., & Norris, J. E. 1991a, *AJ*, **101**, 1835
- Ryan, S. G., & Norris, J. E. 1991b, *AJ*, **101**, 1865
- Schlafly, E. F., & Finkbeiner, D. P. 2011, *ApJ*, **737**, 103
- Schörck, T., Christlieb, N., Cohen, J. G., et al. 2009, *A&A*, **507**, 817
- Scranton, R., Johnston, D., Dodelson, S., et al. 2002, *ApJ*, **579**, 48
- Searle, L., & Zinn, R. 1978, *ApJ*, **225**, 357
- Schlegel, D. J., Finkbeiner, D. P., & Davis, M. 1998, *ApJ*, **500**, 525
- Sills, A., Pinsonneault, M. H., & Terndrup, D. M. 2000, *ApJ*, **534**, 335
- Smolinski, J. P., Lee, Y. S., Beers, T. C., et al. 2011, *AJ*, **141**, 89
- Stetson, P. B. 1987, *PASP*, **99**, 191
- Stoughton, C., Lupton, R. H., Bernardi, M., et al. 2002, *AJ*, **123**, 485
- Tissera, P. B., White, S. D. M., & Scannapieco, C. 2012, *MNRAS*, **420**, 255
- Venn, K. A., Irwin, M., Shetrone, M. D., et al. 2004, *AJ*, **128**, 1177
- Willman, B., Dalcanton, J. J., Martinez-Delgado, D., et al. 2005, *ApJL*, **626**, 85
- Yanny, B., Rockosi, C., Newberg, H. J., et al. 2009, *AJ*, **137**, 4377
- York, D. G., Adelman, J., Anderson, J. E., Jr., et al. 2000, *AJ*, **120**, 1579
- Zucker, D. B., Belokurov, V., Evans, N. W., et al. 2006, *ApJL*, **643**, 103